

# UNVEILING THE $\sigma$ -DISCREPANCY II: REVISITING THE EVOLUTION OF ULIRGS & THE ORIGIN OF QUASARS

BARRY ROTHBERG<sup>1,2,3,4</sup>, JACQUELINE FISCHER<sup>5</sup>, MYRIAM RODRIGUES<sup>6</sup>, D. B. SANDERS<sup>7</sup>

*Draft version February 15, 2013*

## ABSTRACT

We present the first central velocity dispersion ( $\sigma_0$ ) measured from the  $0.85\mu\text{m}$  Calcium II Triplet (CaT) for 8 advanced (i.e. single nuclei) local ( $z \leq 0.15$ ) Ultraluminous Infrared Galaxies (ULIRGs). First, these measurements are used to test the prediction that the “ $\sigma$ -Discrepancy,” in which the CaT  $\sigma_0$  is systematically larger than the  $\sigma_0$  obtained from the  $1.6$  or  $2.3\mu\text{m}$  stellar CO band-heads, extends to ULIRG luminosities. Next, we combine the CaT data with rest-frame  $I$ -band photometry obtained from archival *Hubble Space Telescope* data and the Sloan Digital Sky Survey (SDSS) to derive dynamical properties for the 8 ULIRGs. These are then compared to the dynamical properties of 9,255 elliptical galaxies from the SDSS within the same redshift volume and of a relatively nearby ( $z < 0.4$ ) sample of 53 QSO host galaxies. A comparison is also made between the  $I$ -band and  $H$ -band dynamical properties of the ULIRGs. We find four key results: 1) the  $\sigma$ -Discrepancy extends to ULIRG luminosities; 2) at  $I$ -band ULIRGs lie on the Fundamental Plane (FP) in a region consistent with the most massive elliptical galaxies and not low-intermediate mass ellipticals as previously reported in the near-infrared; 3) the  $I$ -band  $M/L$  of ULIRGs are consistent with an old stellar population, while at  $H$ -band ULIRGs appear significantly younger and less massive; and 4) we derive an  $I$ -band Kormendy Relation from the SDSS ellipticals and demonstrate that ULIRGs and QSO host galaxies are dynamically similar.

**Keywords:** galaxies: evolution—galaxies: formation—galaxies: interactions—galaxies: peculiar—galaxies: kinematics and dynamics—quasars: general

## 1. INTRODUCTION

Questions about the formation and evolution of galaxies are as challenging today as when the 3rd Earl of Rosse first sketched his observations of “external nebulae” (Rosse 1850). Referring to M51, he remarked that their complexity and striking beauty could hardly be the result of static processes. Objects like M51 and the Antennae (NGC 4038/39) have been the focus of astronomical investigations since their appearance in Herschel’s Catalogues of Nebulae and Clusters (Herschel 1786). As photographic plates replaced pencil and paper, surveys continued to catalog peculiar “external nebulae” with ever increasing speculation about their origins (e.g. Pease 1917, 1920; Perrine 1922; Redman & Shirley 1938). Observational work, including morphological classification and measurement of dynamical properties (e.g. Hubble 1930; Zwicky 1956), the first  $N$ -body simulations (e.g. Holmberg 1941) and subsequent numerical simulations (Alladin 1965; Wright 1972) explored the possibility

that peculiar galaxies represented the transformation of galaxies from one form into another by means of interaction.

These earlier works all led directly to the Toomre Hypothesis (Toomre & Toomre 1972; Toomre 1977) which posits that when gas-rich spirals collide and merge together they form a new, more massive elliptical galaxy and that this process is responsible for the formation of all or most ellipticals in the Universe. The gravitational interaction between the two spirals rearranges the stellar orbits from circular to random via violent relaxation (e.g., Lynden-Bell 1967; Hjorth & Madsen 1991). The process of gaseous dissipation funnels gas into the common gravitational center of the coalescing system, which triggers intense star-formation deep within molecular clouds and adds substantial mass to the final remnant (e.g., Barnes & Hernquist 1991; Mihos & Hernquist 1994a, 1996). The most intense mergers are Ultraluminous Infrared Galaxies (ULIRGs), systems with  $L_{\text{IR}}$  ( $8\text{--}1000\mu\text{m}$ )  $\geq 10^{12} L_{\odot}$  (e.g. see Sanders & Mirabel 1996; Sanders 1999; Joseph 1999, for a review). The hypothesis that there is a natural evolution from ULIRG to QSO is based on the idea that gaseous dissipation fuels more than a nuclear starburst. The accretion of both gas clouds and stellar remnants fuels the formation of an active galactic nucleus or AGN (Sanders et al. 1988, hereafter S88). This was further supported by the similarity between the observed bolometric ( $L_{\text{Bol}}$ ) luminosities and space-densities of ULIRGs and QSOs out to at least  $z \sim 0.4$  (Soifer et al. 1986; Canalizo & Stockton 2001). Only after the obscuring medium in the ULIRG is cleared by (presumably) radiation pressure and supernovae explosions does the QSO become visible (e.g.

<sup>1</sup> National Research Council Postdoctoral Fellow at Naval Research Laboratory, Code 7211, 4555 Overlook Ave SW, Washington D.C. 20375, USA

<sup>2</sup> Space Telescope Science Institute, 3700 San Martin Drive, Baltimore, MD 21218, USA

<sup>3</sup> George Mason University, Department of Physics & Astronomy, MS 3F3, 4400 University Drive, Fairfax, VA 22030, USA

<sup>4</sup> Leibniz-Institut für Astrophysik Potsdam (AIP), An der Sternwarte 16, 14482, Potsdam, Germany, brothberg@aip.de, dr.barry.rothberg@gmail.com, current address

<sup>5</sup> Naval Research Laboratory, Code 7211, 4555 Overlook Ave SW, Washington D.C. 20375, USA

<sup>6</sup> European Southern Observatory, Alonso de Cordova 3107, Casilla 19001, Vitacura, Santiago, Chile

<sup>7</sup> Institute for Astronomy, 2680 Woodlawn Drive, Honolulu, HI 96822, USA

Hopkins et al. 2006).

Photometric observations of spiral-spiral mergers, including ULIRGs and their lower luminosity ( $10^{11} L_{\odot} \leq L_{\text{IR}} < 10^{12} L_{\odot}$ ) counterparts, Luminous Infrared Galaxies (LIRGs), demonstrated strong evidence supporting the Toomre Hypothesis. This includes confirmation from optical to near-IR wavelengths that the global surface brightness (SB) profiles of advanced mergers follow the same de Vaucouleurs  $r^{1/4}$  stellar light profile (de Vaucouleurs 1953) that characterizes elliptical galaxies (e.g., Schweizer 1982; Wright et al. 1990; Lutz 1991; Schweizer 1996; Hibbard & van Gorkom 1996; Veilleux et al. 2002; Rothberg & Joseph 2004; Veilleux et al. 2006; Rothberg & Fischer 2010b, hereafter Paper I), in line with predictions from numerical simulations (e.g., Barnes 1988, 1992). Moreover, numerical simulations show that gaseous dissipation during the merger will form a rotating gas disk which undergoes a strong starburst and transforms into a rotating stellar disk (e.g. Barnes & Hernquist 1991; Mihos & Hernquist 1994b; Barnes & Hernquist 1996; Mihos & Hernquist 1996; Barnes 2002; Hopkins et al. 2008). The starburst generates a luminosity spike at small radii,  $r \leq 1$ -2 kiloparsecs (kpc), in the surface brightness profiles of mergers (Mihos & Hernquist 1994a; Springel 2000). This *excess light* was first directly detected in the  $K$ -band SB profiles of mergers, including (U)LIRGs, and found to have  $L_K \sim 10^{9.5-10.5} L_{\odot}$  (Rothberg & Joseph 2004, hereafter RJ04). Hopkins et al. (2008) modeled the same sample and demonstrated that the excess light from younger stars alone could account for 30% of the total stellar mass. (Haan et al. 2011) detected similar excess light at  $H$ -band using *HST* for a larger sample of (U)LIRGs spanning a wider range of merger stages. Their Figure 14 appears to show an evolution of the excess light as a function of the merger stage including what could be peaks at first passage and final coalescence. These properties, taken together with the observed vast quantities ( $10^9$ - $10^{10} M_{\odot}$ ) of cold molecular gas (e.g. Solomon et al. 1992; Bryant & Scoville 1996; Solomon et al. 1997; Scoville et al. 1997; Downes & Solomon 1998; Iono et al. 2005; Greve et al. 2009) and vigorous star-formation rates (e.g., Prestwich et al. 1994; Anantharamaiah et al. 2000, SFR), make ULIRGs prime candidates for the progenitors of giant ellipticals (gEs) and QSO hosts.

However, a significant challenge arose for the Toomre Hypothesis and the S88 scenario when dynamical masses ( $M_{\text{DYN}}$ ) obtained from central velocity dispersions ( $\sigma_{\odot}$ ) using the 1.6 or 2.3  $\mu\text{m}$  CO band-heads (hereafter denoted as  $\sigma_{\odot, \text{CO}}$ ) and imaging at  $H$  (1.6  $\mu\text{m}$ ) or  $K$ -band (2.2  $\mu\text{m}$ ) implied that (U)LIRGs were the progenitors of low to intermediate mass ellipticals (e.g., Shier et al. 1996; Shier & Fischer 1998; James et al. 1999; Genzel et al. 2001; Tacconi et al. 2002; Dasyra et al. 2006). The near-infrared was used because it is less affected by the presence of dust than optical wavelengths. Dunlop et al. (2003) (hereafter D03) compared near-IR photometry, by assuming a fiducial ( $R-K$ ) transformation, with optical imaging of nearby ( $z \leq 0.4$ ) radio loud and radio quiet QSOs (RLQ and RQQ,

respectively)<sup>8</sup>. D03 concluded that the small half-light radii of ULIRGs precluded them as candidates for the progenitors of QSO host galaxies. Veilleux et al. (2006) made a similar comparison using *Hubble Space Telescope* (*HST*) imaging obtained with the Near Infrared Camera and Multi-Object Spectrometer (NICMOS) at  $F160W$  ( $\sim H$ -band) of ULIRGs and Palomar Green (PG) QSOs, along with QSOs from D03 (transformed from  $R$ -band to  $F160W$ ), and relatively nearby ellipticals. They concluded that ULIRGs were the progenitors of 1-2  $L^*$  ellipticals or S0s.

Interestingly, when the Calcium II Triplet stellar absorption lines ( $\lambda \sim 0.85 \mu\text{m}$ ) were used to measure  $\sigma_{\odot}$  (hereafter  $\sigma_{\odot, \text{CaT}}$ ) a very different picture emerged. A comparison between  $\sigma_{\odot, \text{CaT}}$  and  $\sigma_{\odot, \text{CO}}$  in the same set of LIRGs systematically showed  $\sigma_{\odot, \text{CaT}} > \sigma_{\odot, \text{CO}}$  (Rothberg & Joseph 2006a, hereafter RJ06a). Moreover, the  $\sigma_{\odot, \text{CaT}}$  values were consistent with ellipticals over a large mass range, including gEs. Recent work by (Rothberg 2009; Rothberg & Fischer 2010b, hereafter Paper I) has effectively explained this  $\sigma$ -Discrepancy. Paper I compared  $\sigma_{\odot, \text{CaT}}$  with  $\sigma_{\odot, \text{CO}}$  and  $I$ -band photometry with  $K$ -band photometry in advanced LIRG and non-LIRG mergers as well as elliptical galaxies. No  $\sigma$ -Discrepancy was found for elliptical galaxies, a result subsequently confirmed by Vanderbeke et al. (2011). Paper I also showed that in advanced mergers ( $\text{Log } L_{\text{IR}} \leq 11.99$ ), the  $\sigma$ -Discrepancy strongly correlated with  $\text{Log } L_{\text{IR}}$  and dust mass. Although Paper I did not include any ULIRGs in the sample, the results were extrapolated to brighter  $L_{\text{IR}}$ . Paper I concluded that in IR-luminous mergers the near-IR observations are dominated by the presence of a luminous, rotating young central stellar disk (YCSD) which contains a population of Red Supergiant (RSG) or Asymptotic Giant Branch (AGB) stars. Stellar disks have been directly detected in *Hubble Space Telescope* (*HST*) observations of the archetypal merger NGC 7252 (Whitmore et al. 1993) and the LIRG merger NGC 34 (Schweizer & Seitzer 2007), with diameters ranging from 2-6 kpc. These are consistent with the extent of the excess light at  $K$  and  $H$ -band (RJ04, Haan et al. 2011); the observed size of rotating molecular gas disks in mergers (e.g. Dupraz et al. 1990; Wang et al. 1991; Downes & Solomon 1998) and numerical simulations (e.g. Barnes 2002; Hopkins et al. 2008). The rotating YCSD affects the  $\sigma_{\odot, \text{CO}}$  measured in the centers of IR-luminous galaxies, which in turn affects the derived values of  $M_{\text{DYN}}$ . However, at  $I$ -band, the presence of dust, which is more centrally concentrated due to the starburst, behaves like a coronagraph. It masks the bright YCSD so that  $\sigma_{\odot, \text{CaT}}$  reflects *only* the random motions of the old stellar population, probing the galaxy's true  $M_{\text{DYN}}$ . Figures 13-15 in Paper I demonstrated that the red ( $I-K$ ) colors within the central 1.53 kpc could be best explained by many magnitudes of extinction. While at larger radii the ( $I-K$ ) colors (Figure 13 and 14 in Paper I) were consistent with the average colors observed in elliptical galaxies, supporting the proposition that dust is centrally concentrated in IR-luminous mergers. Thus, when viewed at near-IR wavelengths LIRG mergers ap-

<sup>8</sup> The dividing line between radio loud and quiet at 6 cm is  $10^{24} \text{ W Hz}^{-1} \text{ Sr}^{-1}$  (Miller et al. 1990; Stocke et al. 1992; Hooper et al. 1995)

pear to have young stellar populations with  $M_{\text{Dyn}} \leq m^*$ , where  $m^*$  is the *stellar* (not dynamical) mass  $\sim 3 \times 10^{10} M_{\odot}$  (Blanton et al. 2003; Bell et al. 2003). While at  $I$ -band they appear to have older stellar populations and  $M_{\text{Dyn}} > m^*$ .

The results in Paper I provide strong motivation for revisiting the S88 paradigm of whether ULIRGs are massive enough to form gEs and host QSOs. This paper presents the first results for 8 ULIRGs (part of a larger survey) using  $\sigma_{\odot}$  from the CaT stellar absorption lines in conjunction with rest-frame  $I$ -band imaging. We probe two important questions: 1) Does the  $\sigma$ -Discrepancy extend to the more luminous ULIRG population? and 2) At  $I$ -band are the dynamical properties of advanced ULIRGs consistent with gEs, including the host galaxies of QSOs?

All data and calculations in this paper assume  $H_0 = 75 \text{ km s}^{-1} \text{ Mpc}^{-1}$  and a cosmology of  $\Omega_M = 0.3$ ,  $\Omega_{\Lambda} = 0.7$  ( $q_0 = -0.55$ ). All photometric results are in VEGA magnitudes. In this work, ULIRGs are strictly defined as  $L_{\text{IR}} \geq 10^{12.0} L_{\odot}$ . LIRGs are strictly defined as  $10^{11.0} L_{\odot} \leq L_{\text{IR}} \leq 10^{11.99} L_{\odot}$ .

## 2. SAMPLES

### 2.1. ULIRG Sample

The 8 ULIRGs analyzed in this paper were randomly selected (based on observability and available rest-frame  $I$ -band imaging only) from a larger, complete, volume limited ( $z < 0.15$ ) sample of 40 advanced objects taken from the Infrared Astronomical Satellite (IRAS) 1 Jy Survey (Kim & Sanders 1998) and the IRAS Revised Bright Galaxy Sample (Sanders et al. 2003). The IRAS 1 Jy survey is a complete sample of 118 ULIRGs down to flux levels of  $f_{\nu} = 1 \text{ Jy}$  with Galactic latitude  $|b| > 30^\circ$ , declination  $\delta > -40^\circ$  and  $0.02 < z < 0.27$ . The Revised Bright Galaxy Sample is a flux-limited survey of galaxies with a  $60 \mu\text{m}$  flux density  $> 5.24 \text{ Jy}$  covering the entire sky surveyed by IRAS. Late-stage ULIRGs were selected because  $\sigma_{\odot}$  is unlikely to change substantially once the nuclei coalesce (Mihos 1999). Based on numerical simulations and observations it marks the point at which the merger should exhibit properties in common with elliptical galaxies. HST  $F160W$  NICMOS2 images were used to confirm the presence of a single nucleus in each system (within the resolution limits of 59-182 pc). Six of the eight ULIRGs were observed with HST using either the Advanced Camera for Surveys Wide Field Camera (ACS/WFC) or the Wide Field Planetary Camera 2 (WFPC2). Photometric data for the remaining two were obtained from the Seventh Release of the Sloan Digital Sky Survey (York 2000; Abazajian 2009, hereafter SDSS DR7). Optical images of the ULIRGs are shown in Figure 1 of Appendix C. Table 1 lists the basic information: Names, Right Ascension (R.A.), Declination (Dec.), redshift ( $z$ ), Log  $L_{\text{IR}}$ , and Galactic Reddening  $E(B - V)$ .  $L_{\text{IR}}$  is defined as the total flux from 8-1000  $\mu\text{m}$  (Sanders & Mirabel 1996) using the four IRAS passbands (12, 25, 60 and 100  $\mu\text{m}$ ). However, supplemental 12 or 22  $\mu\text{m}$  photometry from the Wide-Field Infrared Survey Explorer was used in several cases where IRAS did not detect the ULIRG (see notes in Table 1).

### 2.2. Comparison Samples

#### 2.2.1. SDSS $i$ -band DR7 Elliptical Sample

In order to assess the significance of the optically measured values of  $\sigma_{\odot, \text{CaT}}$  and masses of ULIRGs, a comparison sample of elliptical galaxies was assembled from the SDSS DR7 which offers larger spectroscopic and photometric coverage over earlier releases and improvements in photometric and spectroscopic measurements. The comparison sample was selected to be volume limited ( $z \leq 0.15$ ) to match the ULIRG sample. A total of 9,255 elliptical galaxies were extracted from the SDSS using the selection criteria detailed in Appendix A. The selection criteria required that the elliptical galaxy must be present in both the photometric and spectroscopic databases.

#### 2.2.2. Radio Loud and Radio Quiet QSOs

A relatively nearby ( $0.08 < z < 0.46$ ) comparison sample of 28 RLQ and 25 RQQ host galaxies was compiled from available photometry obtained with WFPC2 on HST and ground-based kinematic data. Only QSOs with confirmed elliptical host morphology were selected from the samples of Bahcall et al. (1997); Hamilton et al. (2002); Dunlop et al. (2003); Floyd et al. (2004); Hamilton et al. (2008). The source papers all note that their samples were designed so that: 1) the RLQ and RQQ subsamples are matched in terms of optical luminosity; 2)  $M_V < -23$ , representing  $L \geq L^*$  galaxies and ensuring that QSOs were selected; and 3) at  $z \sim 0.4$  the resolution of the WFPC2 cameras were sufficient to separate host from nucleus. In all cases the authors of the source papers performed extensive point spread function (*PSF*) modeling using separate stellar observations to properly subtract the nucleus from the host. Although the assembled comparison sample of QSO host galaxies is heterogeneous, each of the source papers have demonstrated that their samples are statistically representative of the local QSO host galaxy populations. Moreover, the selection criteria employed by the source papers are remarkably similar with significant overlap. The D03 and Floyd et al. (2004) (hereafter F04) samples are subsamples from McLure et al. (1999) at  $0.1 < z < 0.35$ , while the sample from Hamilton includes nearly all of the D03 sources, selected so that  $0.06 < z < 0.4$ . The total integration times of all of the QSO observations were checked with the latest version of the WFPC2 exposure time calculator to ensure they were sufficiently deep to properly sample the underlying host galaxy. The basic information for the comparison sample of RLQs and RQQs are listed in Columns 1-6 of Table B1 in Appendix B.

## 3. OBSERVATIONS AND DATA REDUCTION

### 3.1. Optical $F814W$ Images

The optical  $F814W$  filter was selected because the same filter was used for the  $I$ -band study in Paper I. That paper demonstrated that the  $F814W$  filter is the best compromise between observing the old stellar population, which is used to probe the total  $M_{\text{Dyn}}$ , and avoiding light produced by RSG and AGB stars. Here, and in Paper I the  $F814W$  filter is simply referred to as  $I$ -band. The mean differences among the ACS  $F814W$ , the WFPC2  $F814W$ , and the Cousins  $I$ -band filters are less than a few hundredths of a magnitude.  $F814W$  images of

6 ULIRGs were obtained from the public *HST* archives (see Table 2 for more information).

Five of the ULIRGs were observed with ACS/WFC as part of the Great Observatories All-Sky LIRG Survey (Armus et al. 2009). ACS/WFC is comprised of two  $4096 \times 2048$  pixel CCDs, each with a platescale of  $0''.049 \text{ pixel}^{-1}$ , providing a field of view (FOV)  $\sim 202'' \times 202''$ . This FOV is large enough to observe each of the 5 ULIRGs completely. There is a gap of 50 pixels ( $2''.45$ ) between the two CCDs. The observations employed a two position dither to fill the chip gap rather than the more common CR-SPLIT (two images taken at the same position) which is better for cosmic ray (CR) removal but leaves the gap with no data. As in Paper I, the ACS/WFC data were processed manually using the Image Reduction and Analysis Facility<sup>9</sup> (IRAF) and the Space Telescope Science Data Analysis System (STSDAS), which is a software package designed specifically for the reduction and analysis of HST data that works with IRAF. Individual exposures which have been calibrated and flat field corrected were obtained from the archives for the 5 ULIRGs observed with ACS/WFC. For each ULIRG, the STSDAS task MULTIDRIZZLE was used to assemble individual dithered frames into a final mosaic image corrected for: geometric distortions and CRs; bad pixels set to a value of zero; and rotated to a position angle (P.A.) of  $0^\circ$ . This differs from the final drizzled image produced by the archive pipeline. Three bad pixels were found in the center of IRAS 05189-2524 due to CR hits and warm pixels, and not due to saturation from over-exposure. The IRAF pixel editing task IMEDIT was used to replace the zeroed pixels with the values interpolated from the surrounding pixels. The central region of IRAS 12540+5708 was found to be saturated. Both the diffraction spike generated from the bright core and a  $12 \times 14$  pixel rectangle in the center of IRAS 12540+5708 were saturated. These were flagged by MULTIDRIZZLE and set to a value of zero. No images with shorter exposures were available to replace the flagged pixels and they were ignored in the subsequent analysis. Due to the two position dithering scheme used, MULTIDRIZZLE was unable to flag and remove a large number of CRs, particularly within the chip gap. Because the targets were centered in the ACS/WFC FOV, the chip gap runs through or close to the outer regions of the ULIRGs. As a result an algorithm was developed to remove CRs and is detailed in Appendix D.

One ULIRG, IRAS F02021-2103, was observed with WFPC2, which is comprised of four  $800 \times 800$  pixel CCDs. Three of the chips (WF2, WF3, and WF4) have a platescale of  $0''.099$  and the fourth (PC)  $0''.046$ . This creates a non-symmetric FOV with a gap in coverage in the upper right quadrant. The observations for IRAS F02021-2103 were centered on the WF3 chip. The observations were reduced using calibrated and flat field corrected WFPC2 science images obtained from the *HST* archives and processed with the STSDAS tasks WARMPIX, which fixes hot pixels, and CRREJ, which removes CRs and combines multiple frames into a single image. Geo-

metric distortions were corrected by multiplying the CR cleaned image with a correction image (Holtzman et al. 1995). Finally, the image was trimmed to remove pixels vignettted by the pyramid shaped beam-splitter mirror.

### 3.2. Near-Infrared F160W Images

The *F160W* filter was selected because no similarly deep *K*-band data were available (as used in Paper I) and because the CO band-heads at  $1.6 \mu\text{m}$  were used for many objects to measure  $\sigma_{\text{O,CO}}$ . Published or archival data were used only for the 5 ULIRGs with published values of  $\sigma_{\text{O,CO}}$ . All observations used NICMOS with the NIC2 camera, a  $256 \times 256$  pixel HgCdTe array with  $0''.075 \text{ pixel}^{-1}$  platescale ( $19''.2$  FOV). Photometric data for 3/5 ULIRGs were obtained from the literature. IRAS 17208-0014 and IRAS 23365+3604 were analyzed from *HST* archival data.

The NIC2 data were processed manually using IRAF and STSDAS. The *raw* (data received directly from the spacecraft without processing) files were used rather than the archive processed data in order to properly account for: 1) the presence of the NIC2 coronagraph; 2) the presence of bias jumps between the quadrants; and 3) the presence of electronic “bars” which appear as vertical stripes. The coronagraph shifts position over time and the anomalies vary with time requiring the individual raw frames to be processed manually. First, the STSDAS task CALNICA was used to subtract dark current, correct for detector non-linearity, flatfield, convert to count rates, and identify and reject CRs. Next, the STSDAS task PEDSUB was used to correct for bias jumps between quadrants. This differs from the standard archival pipeline reduction which uses PEDSKY to remove both bias jumps and sky background. Because the objects fill most of the NIC2 array, using PEDSKY will result in a non-uniform over-subtraction of the background. In cases where electronic bars and other anomalies were found in individual raw frames, the STSDAS task NICPIPE was used instead. It allows the user to apply some or all of the steps from CALNICA. In this case, all steps except flat-fielding, conversion to count-rates, and CR rejection were applied to the data. Next the data were processed with BIASEQ, which corrects for drift in the bias levels during the course of MultiAccum exposures. The data were then processed through NICPIPE again, this time applying flatfields, conversion to count-rates and cosmic-ray rejection. The position of the coronagraph was determined in each individual frame and masked using the IRAF task IMEDIT. Other bad columns and hot pixels not removed with CALNICA or NICPIPE were manually identified and masked with the IRAF task IMEDIT. The frames were then processed with MULTIDRIZZLE in the same manner as the ACS/WFC *F814W* data above, producing geometrically corrected images rotated to a P.A. of  $0^\circ$ . A comparison between this method and data pre-processed through the standard archive pipeline showed a significant improvement in signal to noise (S/N), including the detection of faint tidal features which would otherwise not be visible.

### 3.3. Spectroscopy

The optical spectra for all of the ULIRGs presented here were obtained with the Echelle Spectrograph and

<sup>9</sup> IRAF is distributed by the National Optical Astronomy Observatory, which is operated by the Association of Universities for Research in Astronomy, Inc., under cooperative agreement with the National Science Foundation.

Imager (Sheinis et al. 2002, ESI) in echelle mode at the W.M. Keck II 10m observatory. Echelle mode employs a  $20''$  long slit and cross-dispersed spectra with simultaneous coverage of  $0.3927\text{--}1.1068\mu\text{m}$  projected onto a  $2048 \times 4096$  pixel CCD. ESI has a fixed spectral resolution of  $11.5 \text{ km s}^{-1} \text{ pixel}^{-1}$ . The final spectral resolution scales with slit width. A  $1''.0$  slit width (6.49 pixels) was used for 7/8 ULIRGs. This corresponds to  $R \sim 4000$  or  $\sim 75 \text{ km s}^{-1}$ . A  $0''.5$  slit width (3.24 pixels) was used for IRAS 12540+5708. This corresponds to  $R \sim 8300$  or  $\sim 37 \text{ km s}^{-1}$ . In this paper only spectral orders containing the CaT stellar absorption lines (order 6 or 7 depending on redshift) were used. The scale along the spatial axis for order 6 and 7 are  $0''.168$  and  $0''.163$ , respectively. The integration time and P.A. for each ULIRG is listed in Table 2. Calibrations, including internal flats and Hg-Ne, Xe, and CuAr arcs were taken at the beginning and end of the night. No changes were detected between flats and arcs taken at the start and end of night. ESI spectra for three ULIRGs (IRAS 05189-2524, IRAS F10378+1108, and IRAS 11387+4116) were first presented in Rupke et al. (2002) but did not include CaT  $\sigma$  measurements.

The data were reduced with IRAF. The reduction of the data and spectral extraction method used are nearly the same as those described in Section 3.1 of Paper I (e.g. correction to heliocentric rest velocities, spectrophotometric correction to remove instrumental signature and provide approximate flux calibration, continuum normalization, and generation of the error spectrum). The few differences with the methodology used in Paper I are described here. Due to the redshifts of the ULIRGs the CaT lines lie at wavelengths within a spectral region dominated by strong night-sky emission lines. This was corrected using the IRAF task **BACKGROUND** which measures a sky spectrum at both edges of the slit and fits it with a polynomial (in this case a 1st or 2nd order Chebyshev polynomial) which is then subtracted from the spectrum. The polynomial fitting and subtraction is carried out column by column. In one case, the redshift of IRAS F02021-2103 placed the CaT absorption lines coincident with some telluric absorption lines. The IRAF task **TELLURIC** was used to correct for the presence of the telluric absorption lines using a featureless spectrophotometric standard star.

The spectra of 5/8 ULIRGs were extracted in a metric aperture of diameter 1.53 kpc (see Table 3). This size was selected to remain consistent with the literature (e.g. Jorgensen et al. 1995; Smith et al. 1995; Pahre et al. 1998a; Pahre 1999; Rothberg & Joseph 2006a,b, hereafter RJ06b, and Paper I.) However, in order to maximize S/N, larger diameter apertures of size 3.77 kpc and 4.05 kpc were used to extract the spectra of IRAS F10378+1108 and IRAS 11387+4116, respectively. Due to the brightness of the IRAS 12540+5708 nucleus, the spectrum was extracted in a 0.82 kpc diameter aperture 2.08 kpc northwest of the nucleus. This is several times larger than the seeing of the observations, well within the region dominated by stellar continuum (Davies et al. 2004), and the same method used by Tacconi et al. (2002); Dasyra et al. (2006) to measure  $\sigma_{\text{CO}}$ . Finally, the IRAF task **CONTINUUM** was used to identify and remove residual sky lines present from imperfect background subtraction in IRAS 17208-0014,

IRAS 19542+1110, and IRAS 23365+3604.

#### 4. DATA ANALYSIS

##### 4.1. Photometry

###### 4.1.1. Galactic Reddening

Photometry for all ULIRGs (*HST* and SDSS), comparison ellipticals and QSO host galaxies have been corrected for Galactic reddening using  $E(B-V)$  values from Schlegel et al. (1998) as presented in NED<sup>10</sup> and assume  $R_V = 3.1$  (Fitzpatrick 1999). These values were then scaled to the appropriate photometric filters: *F814W* and *z* for the ULIRGs; and the native filters listed in Table B1 for the QSO host galaxies using values from (Schlafly & Finkbeiner 2011). Scaling factors for the *F675W* and *F791W* filters were computed using the York Extinction Solver (McCall 2004). The values used are listed in Tables 3, 4, and B1.

###### 4.1.2. Measured Global Photometric Parameters

Photometry was performed on the *F814W* images from ACS/WFC and WFPC2/WF3 and the *F160W* images from NIC2 to measure the global photometric parameters: the effective (or half-light) radius  $R_{\text{eff}}$  measured in metric units of kpc, the mean surface brightness *within* the effective radius ( $\langle \mu \rangle_{\text{eff}}$ ), and the total absolute magnitude ( $M_I$  or  $M_{F160W}$ ). The fluxes were measured in circular isophotes with fixed centers using the STSDAS task **ELLIPSE**. The position of the galaxy centers in the *F814W* images were determined from *F160W* NIC2 images. As in Paper I, there were several cases where the nucleus was clearly visible in the *F160W* images but obscured or partially obscured in the *F814W* images. Foreground stars, bad pixels, artifacts or CRs missed by **MULTIDRIZZLE** were masked with a bad pixel mask created using the technique described in Appendix D. Masked items were set to a value of zero and ignored in the isophote fitting and flux measurements. An  $r^{1/4}$  de Vaucouleurs profile was fit to the isophotes produced by **ELLIPSE** for each galaxy. These surface brightness profiles are plotted in Figure 2 of Appendix C. The angular effective radius (in arcseconds) from the de Vaucouleurs profile was converted to  $R_{\text{eff}}$  using the angular diameter and co-moving distance for our preferred cosmology. The values of  $\langle \mu \rangle_{\text{eff}}$  were derived from the  $r^{1/4}$  profile fits and were corrected for cosmological dimming (Tolman 1930). The total  $M_I$  or  $M_{F160W}$  were computed by extrapolating the best-fit de Vaucouleurs model beyond the measured data and using the luminosity distance for our preferred cosmology.

Table 3 lists the  $M_I$ ,  $R_{\text{eff}}$  and  $\langle \mu_I \rangle_{\text{eff}}$  values for the ULIRGs in the *F814W* filter. Table 4 lists the measured values of  $R_{\text{eff}}$  at *F160W* and  $M_{F160W}$  for IRAS 17208-0014 and IRAS 23365+3604. *F160W* photometric results for IRAS F02021-2103, IRAS 05189-2524, and IRAS 12540+5708, in Table 4 were obtained from Veilleux et al. (2006). For each of these ULIRGs, the sources were checked to ensure that an  $r^{1/4}$  profile was the better fit to the surface brightness profile. The values of *F160W*  $R_{\text{eff}}$  were converted to *equivalent radii*,

<sup>10</sup> The NASA/IPAC Extragalactic Database (NED) is operated by the Jet Propulsion Laboratory, California Institute of Technology, under contract with the National Aeronautics and Space Administration.

which is the equivalent circular radius for measurements originally made with elliptical isophotes. The equivalent radii were computed using the semi-major and semi-minor axes, or the semi-major axis and ellipticity (e.g. Milvang-Jensen & Jørgensen 1999).

#### 4.1.3. Global Photometric Parameters of ULIRGs and Elliptical Galaxies from the SDSS

No data reduction was performed on the actual SDSS DR7 images. Photometric data for IRAS F10378+1108 and IRAS 11387+4116 were extracted from the SDSS DR7. The Sloan  $z$ -band filter was selected over the Sloan  $i$ -band filter based on two factors:

- 1) At the redshifts of IRAS F10378+1108 and IRAS 11387+4116 the Sloan  $z$  filter overlaps the rest-frame wavelength coverage of the  $F814W$  filter;
- 2) Because the wavelength coverage of the Sloan  $i$ -filter is bluer than the Cousins  $I$  and  $F814W$  filters, at these redshifts flux from strong emission lines of [OI],  $H\alpha$ , [NII], and [SII] could contribute significantly to the total observed flux for each galaxy. At the same time, the observed wavelength coverage of the  $z$ -band filter is now blue-ward of possible contamination from [SIII] at 0.9069 and 0.9531  $\mu\text{m}$ .

The metric equivalent radius for  $R_{\text{eff}}$  was computed from the SDSS parameters **devRad**, the half-light semi-major radius measured from a de Vaucouleurs fit to the galaxy light; and **devAB**, the axis ratio from the de Vaucouleurs best fit profile. Criteria 7 in Appendix A, that a galaxy is better represented by a de Vaucouleurs profile rather than an exponential profile, was verified for the two ULIRGs. Values of  $\langle\mu_z\rangle_{\text{eff}}$  were computed from the SDSS parameters **devMag**, the total apparent magnitude measured from the de Vaucouleurs fit to the galaxy light convolved with a double-Gaussian fit to the PSF; and the angular equivalent radius  $r_{\text{eff}}$  (e.g. equation 7 in Hyde & Bernardi 2009b, hereafter HB09) and includes corrections for cosmological dimming.  $M_z$  was also computed from **devMag** using the luminosity distance for our preferred cosmology.

The **devMag** fluxes were converted from AB magnitudes to VEGA magnitudes using the task **CALCPHOT** which is a part of the SYNPHOT (synthetic photometry) program in STSDAS (Horne 1988; Koornneef et al. 1986; Laidler et al. 2005). **CALCPHOT** calculates synthetic photometry for any input spectra or blackbody curves using any filter transmission curve. It can be used to calculate  $k$ -corrections and transformations between filters. A transformation value of  $(z_{\text{VEGA}} - z_{\text{AB}}) = -0.51$  was used. Due to large variations in the rest-frame ultraviolet and optical spectral energy distributions (SEDs) the  $k$ -corrections for ULIRGs at  $z \sim 0.1$  can vary by  $\Delta \pm 0.01$ - $0.09$  mags (e.g. Surace et al. 1998; Trentham et al. 1999). Therefore, no  $k$ -corrections were applied to the two ULIRGs. Although the same spectral regions are covered by the redshifted SDSS  $z$  filter and the rest-frame  $F814W$  filter, the shape of the filter transmission curves for the two filters are very different. To assess the impact of this, we tested **CALCPHOT** with 12 spectral templates: an elliptical, S0, Sa, and Sb galaxies (Kinney et al. 1996); six different starburst galaxies with variations in the amount of extinction (Calzetti et al. 1994), including extinction similar to those observed in ULIRGs; and a composite spectrum of the Seyfert 2 NGC 1068, which includes ul-

traviolet and optical lines, nebular and power-law continuum and cool stars (Laidler et al. 2005). **CALCPHOT** yielded  $(F814W - z) = 0.19 \pm 0.01$  and  $0.18 \pm 0.01$  for IRAS F10378+1108 and IRAS 11387+4116, respectively. The small dispersion among the different templates is due to the similarity of the spectral features within the rest-frame  $F814W$  wavelength range. These additional transforms were also applied to the values of **devMag**. For the remainder of the paper the observed Sloan  $z$  values for IRAS F10378+1108 and IRAS 11387+4116 will be referred to as  $I$ -band. Table 3 lists the computed  $M_I$ ,  $R_{\text{eff}}$  and  $\langle\mu_I\rangle_{\text{eff}}$  values for IRAS F10378+1108 and IRAS 11387+4116.

Global photometric parameters for the SDSS ellipticals were computed in a similar fashion using the SDSS DR7  $i$ -band values for **devMag**, **devRad**, **devAB**, redshift, and extinction values.  $k$ -corrections and a filter transformation from SDSS  $i$ -band to  $F814W$  filter were computed using **CALCPHOT** and an elliptical galaxy template spectrum (Kinney et al. 1996). The  $k$ -corrections ranged from 0.03-0.16 mags with a filter transform of  $(F814W_{\text{VEGA}} - i_{\text{ABMAG}}) = -0.59$ . Due to the large size of the SDSS elliptical sample, the computed photometry is not presented in the paper, but the selection criteria is provided in Appendix A and can be used to retrieve the sample from the SDSS DR7.

#### 4.1.4. RLQ & RQQ Host Galaxies

The details of the data reduction methods used for these galaxies can be found in Bahcall et al. (1997); Hamilton et al. (2002); Dunlop et al. (2003); Floyd et al. (2004); Hamilton et al. (2008). The samples published in these papers were observed with WFPC2 on *HST* using the  $F606W$ ,  $F675W$ ,  $F702W$ ,  $F791W$ , or  $F814W$  filters. The source papers provide surface brightnesses at the effective radius ( $\mu_{\text{eff}}$ ), not surface brightness *within* the effective radius ( $\langle\mu_I\rangle_{\text{eff}}$ ), and absolute and apparent magnitudes of each host galaxy and nucleus or *PSF*. In the source papers, these values were transformed from their observed filters to either rest-frame Johnsons  $V$  or Cousins  $R$ -band magnitudes. To avoid adding additional uncertainties to the analysis, only the apparent magnitudes of the host galaxies in the original *HST* filters were used. They were  $k$ -corrected and transformed to rest-frame  $F814W$  magnitudes using **CALCPHOT** with an elliptical galaxy template (Kinney et al. 1996). An elliptical template was selected because all of the QSO host galaxies have confirmed elliptical galaxy morphologies and observations of the host galaxy spectra for nearly half of the sample indicate they are dominated by the presence of an older, quiescent stellar population at optical wavelengths (Hughes et al. 2000; Canalizo & Stockton 2000; Nolan et al. 2001; Letawe et al. 2007; Wold et al. 2010).

With the exception of Bahcall et al. (1997) the published values of  $R_{\text{eff}}$  for the QSO host galaxies were measured from elliptical isophotes. These were transformed to equivalent radii using ellipticities or semi-major and minor axes from the source papers and Hamilton (*private communication*) and converted to metric values of  $R_{\text{eff}}$  using our preferred cosmology. These, along with the transformed  $F814W$  apparent magnitudes were used to compute  $\langle\mu_I\rangle_{\text{eff}}$  in the same way as for the SDSS galaxies.  $M_I$ ,  $R_{\text{eff}}$  and  $\langle\mu_I\rangle_{\text{eff}}$  are listed in Columns 8-10 of Table B1.

## 4.2. Velocity Dispersions

### 4.2.1. Measurement of $\sigma_o$

The details of the method used to measure  $\sigma_o$  from the extracted one-dimensional ESI spectra are given in RJ06a, RJ06b and Paper I. The IDL routine **VELOCDISP** described in those papers and used here is based on a pixel-space direct fitting method to measure  $\sigma_o$ . This method is similar to the technique described in Rix & White (1992). Briefly, the template stars are convolved with a Gauss-Hermite Polynomial, which is a modified Gaussian (van der Marel & Franx 1993). The 18 template stars used for the fitting range from G1 to M7.5 giants to K1 to M5 supergiants (see Table 4 in Paper I) and are the same stars used in Paper I for the CaT and 2.3  $\mu\text{m}$  CO spectra. The fitting function has five parameters: the line strength ( $\gamma$ ), which measures the ratio of the equivalent width of the galaxy to that of the template star; the mean recession velocity ( $v_o$ ), the central velocity dispersion ( $\sigma_o$ , defined as  $\sigma$  in a 1.53 kpc metric aperture), the skewness ( $h_3$ ), and kurtosis ( $h_4$ ). The last two parameters characterize the departures from a Gaussian shape. The parameters are simultaneously fit to the data over the wavelength range 0.8480-0.8690  $\mu\text{m}$  (Barth et al. 2002). Bad pixel masks were used to mask out strong emission lines or regions of imperfect background subtraction. Table 3 shows the best-fit results for the derived  $\sigma_o$ , heliocentric recessional velocity ( $V_o$ ) and best-fit template star for each ULIRG. The errors in Tables 4 were calculated by **VELOCDISP** using the error spectrum for each galaxy. A more detailed discussion of this method of error analysis and a comparison with Monte Carlo simulations can be found in RJ06a, RJ06b, and Paper I. Figure 3 in Appendix C shows the CaT spectra for the eight ULIRGs (solid line), over-plotted with the best-fit convolved stellar template (gray dashed line).

### 4.2.2. Aperture Corrections

In order to reduce possible errors introduced by measuring kinematic properties in different aperture sizes, the values of  $\sigma_o$  reported in this paper are either initially measured in a common aperture diameter of 1.53 kpc or corrected to this aperture size (see Tables 3, 4, and B2). This also applies to all published velocity dispersions, including the QSO host galaxies, SDSS ellipticals, and the CO velocity dispersions of ULIRGs. The corrections used the scaling relation from Jorgensen et al. (1995):

$$\log \frac{\sigma(d)}{\sigma(d_o)} = \alpha \log \frac{d}{d_o} \quad (1)$$

where  $\alpha = -0.04^{11}$ ,  $d_o = 1.53$  kpc and  $d$  is the metric diameter of the circular aperture. This is directly applicable to the SDSS ellipticals measured in a 3'' diameter circular fiber. In the case of slit spectroscopy for the QSOs and ULIRGs,  $d$  is computed via:

$$d \simeq 1.025 \times 2 \sqrt{\frac{xy}{\pi}} \times n \quad (2)$$

where  $x$  and  $y$  are slitwidth and extraction aperture,  $n$  is the metric scale (pc or kpc) in 1'' for the galaxy computed from the angular diameter. The weighted average

radius along the summed portion of the slit for each QSO was taken from Table 3 in Wolf & Sheinin (2008) and the slitwidths for the CO observations of the ULIRGs from obtained from the relevant source papers (see Table 4).

## 5. RESULTS

The results here first address whether the  $\sigma$ -Discrepancy extends to ULIRG luminosities, as suggested by Paper I. We then test the predictions of the S88 paradigm by using a combination of rest-frame  $I$ -band photometric data and  $\sigma_{o,CaT}$  to assess whether the *global* dynamical properties of the ULIRGs are consistent with those of massive ellipticals, including the host galaxies of QSOs, and whether they exhibit the same significant differences between optical and near-IR properties.

### 5.1. Extending the $\sigma$ -Discrepancy to ULIRGs

A key result from Paper I was a demonstration that in advanced LIRG mergers,  $\sigma_{o,CaT}$  is systematically larger than  $\sigma_{o,CO}$ . The same systematic discrepancy was not observed in bonafide elliptical galaxies (Paper I, Vanderbeke et al. 2011). Paper I further posited that the  $\sigma$ -Discrepancy should also extend to ULIRG luminosities. We now test this hypothesis by comparing the values of  $\sigma_{o,CaT}$  with published values of  $\sigma_{o,CO}$ . Figure 1 shows the five ULIRGs in the sample which have published values of  $\sigma_{o,CO}$  (see Table 4) compared with their  $\sigma_{o,CaT}$  presented in this paper (see Table 3). The dotted line represents  $\sigma_{o,CaT} = \sigma_{o,CO}$ . Taking into account the errors, the  $\sigma_{o,CaT}$  values plotted for the 5 ULIRGs lie 2.5-22.9 $\sigma$  away from the expected  $\sigma_{o,CO}$  values. The relative difference between  $\sigma_{o,CaT}$  and  $\sigma_{o,CO}$  for each galaxy was characterized in Paper I by the parameter  $\sigma_{\text{Frac}}$ :

$$\sigma_{\text{Frac}} = \frac{\sigma_{o,CaT} - \sigma_{o,CO}}{\sigma_{o,CaT}} \quad (3)$$

This parameter was then compared with  $\text{Log } L_{\text{IR}}$  (Figure 4 in Paper I) for both advanced mergers and bonafide elliptical galaxies.  $L_{\text{IR}}$  seems a natural starting point for comparison, given that the degree of the  $\sigma$ -Discrepancy appears to be greater for LIRGs than non-LIRGs, and non-existent in the control sample of ellipticals (Figure 1 of Paper I). The comparison between  $\sigma_{\text{Frac}}$  and  $\text{Log } L_{\text{IR}}$  was quantified using the Pearson Correlation coefficient ( $r$ ) which tests the degree of linear correlation between two independent data sets. The value of  $r$  ranges from -1 to +1 (anti-correlation to perfect positive correlation). In Paper I, a comparison was made for the entire sample of advanced merger remnants ( $9.51 < \text{Log } L_{\text{IR}} < 11.96$ ), yielding a value of  $r = 0.77$  (a strong correlation). The comparison sample of ellipticals in Paper I showed no correlation ( $r = 0.06$ ). In order to determine whether this correlation extends to ULIRG luminosities plotted in Figure 2 are  $\sigma_{\text{Frac}}$  and  $\text{Log } L_{\text{IR}}$  values for the 5 ULIRGs from this paper and all advanced mergers from Paper I. The correlation in Figure 2 is  $r = 0.75^{\pm 0.02}$ . The errors on this correlation were computed using a ‘‘jackknife’’ resampling method (Tukey 1958) in which the computation of the Pearson Correlation for the sample of  $n$  pairs of data points is done using  $n - 1$  pairs of data points. This allows for  $n$  computations of the Pearson Correlation to be made and a standard deviation to be computed to

<sup>11</sup> RF10 has a typographical error that reads  $\alpha = 0.04$  instead of -0.04

test the robustness of the correlation (i.e. that one point may drive an apparent correlation).

The algorithm **FITEXY** was applied to the galaxies in Figure 2. It employs a double-weighted least-squares (DWLSQ) fit using a  $\chi^2$  minimization method that accounts for errors in both variables (Press et al. 1992; Feigelson & Babu 1992). The result is:

$$\sigma_{\text{Frac}} = 0.18^{\pm 0.01} \text{Log } L_{\text{IR}} - 1.79^{\pm 0.11} \quad (\text{Log } L_{\text{IR}} \geq 9.5) \quad (4)$$

This is similar to Equation 7 in Paper I<sup>12</sup>. The  $\text{Log } L_{\text{IR}} - \sigma_{\text{Frac}}$  correlation first shown in Paper I extends to ULIRG luminosities, i.e. the relative difference between  $\sigma_{\text{o,CaT}}$  and  $\sigma_{\text{o,CO}}$  grows with larger  $L_{\text{IR}}$ .

## 5.2. The Dynamical Properties of ULIRGs

### 5.2.1. The Fundamental Plane

Figure 3 shows the *I*-band Fundamental Plane edge on (diagonal solid line). It is a two-dimensional plane embedded within the three-dimensional parameter space of  $\sigma_{\text{o}}$ ,  $R_{\text{eff}}$ , and  $\langle \mu \rangle_{\text{eff}}$  (Djorgovski & Davis 1987). Early-type galaxies lie on the FP, late-type galaxies do not. A relationship similar to the FP can be derived from the Virial Theorem (e.g. Faber et al. 1987; Djorgovski et al. 1988; Bender et al. 1992). The FP can be used as a diagnostic tool to probe whether the dynamical properties of a particular galaxy, or group of galaxies are similar to those of elliptical galaxies. In this section the two fundamental goals are: 1) to ascertain whether the advanced ULIRGs lie on or close to the FP; and 2) to compare where the ULIRGs lie relative to the QSO host galaxies.

The FP plotted in Figure 3 is from the orthogonal fit in Table 2 of HB09 and was derived from  $\sim 50,000$  early-type galaxies ( $z \leq 0.36$ ) using photometry from SDSS Data Release 4 and values of  $\sigma$  from SDSS Data Release 6 (see Hyde & Bernardi 2009a, for more details). As noted in Appendix A, we used the same parameters as HB09 to select the comparison sample of ellipticals but with tighter restrictions on morphology in order to select only ellipticals and exclude S0 galaxies. Thus, it is a sub-sample of HB09.

The Sloan *i*-band was transformed to  $H_{\text{o}} = 75$  and to the *HST* ACS/WFC *F814W* filter using the same method described in Section 4.1.3. In Figure 3, and subsequently for all comparisons, ULIRGs are plotted as filled circles, RQQs as open flattened diamonds, RLQs as open squares, and the SDSS ellipticals are plotted in four groups based on their values of  $\sigma_{\text{o}}$  (see Figure 3 caption). The first group roughly corresponds to sub- $m^*$  ellipticals, the second to  $\sim m^*$  ellipticals and the last two to progressively more massive systems. This adds an additional dimension of information to these plots; and in the case of Figure 3 separates the two parameters which comprise the x-axis, revealing a gradient of increasing  $\sigma_{\text{o}}$  from left to right across the FP. This gradient reflects a previously reported steepening of the slope of the FP as a function of  $\sigma_{\text{o}}$  (e.g. Jorgensen et al. 1996; Bernardi et al. 2003a, HB09). Also of note is an appar-

ent thickening and slight warp or curvature of the FP at small  $R_{\text{eff}}$  and low  $\sigma_{\text{o}}$  which is not due solely to observational errors (Jorgensen et al. 1996; Bernardi et al. 2003a; Nigoche-Netro et al. 2009, HB09).

To determine if ULIRGs lie on or close to the FP, the scatter of the residuals or *r.m.s.* of the ULIRG sample relative to the FP is compared with those of the SDSS Ellipticals. By definition, these ellipticals lie on the FP because they are a sub-sample of the early-type galaxies used to construct the FP itself. The SDSS ellipticals have *r.m.s.* = 0.18 dex (in units of kpc), while the ULIRGs have *r.m.s.* = 0.29 dex. The residuals of the ULIRGs range from -0.72 to 0.30 (the SDSS ellipticals range from -0.68 to 0.40), with a mean and median of -0.05 and 0.04, respectively, indicating no systematic offsets for the sample. In general, the ULIRGs lie well within the scatter of the SDSS ellipticals, with four lying on the FP (within their errors). We conclude that the ULIRGs lie on or close to the FP like bonafide ellipticals. We note that IRAS 19542+1110 is  $3.9\sigma$  from the FP, making it an outlier, although there are SDSS ellipticals which are similarly distant from the plane.

Where do ULIRGs lie on the FP and how does their location compare with those of gEs, including QSO host galaxies? To quantify this, we used a variation of the Kolmogorov-Smirnov (KS) two-sided (i.e. comparison between two empirical distributions) test which is applicable to two-dimensional data sets (Peacock 1983; Fasano & Franceschini 1987; Press et al. 1992). The KS test itself probes the Null Hypothesis that the two distributions to be compared have the same distribution. It is a non-parametric test, meaning no assumption is made about the form of the distribution except that it must be continuous (e.g. Massey 1951). A standard rejection threshold of 95% (also known as the 0.05 confidence level) was selected (Fisher 1925, 1990) for the analysis. If the Null Hypothesis can be rejected at a greater confidence it will be stated, otherwise a statement of rejection or non-rejection will always refer to the 95% level. The two-dimensional form of the KS two-sided test was designed to test the empirical distribution of data points on a plane and provide a goodness-of-fit statistic without the problems which arise from binning (i.e.  $\chi^2$  test) or assumption of a particular shape to the distribution. The test statistics were computed using the methods outlined in Press et al. (1992) which are in turn, based on modifications to the KS statistic (Stephens 1970). These allow for computation of the 2D statistic beyond the limited case examples provided in Fasano & Franceschini (1987). We note two important caveats for the KS tests used here and throughout the remainder of Sections 5.2.1 and 5.2.2. First, the reported errors for the RLQ values of  $\sigma_{\text{o}}$  listed in Table B2 are significantly larger ( $\pm 17$ -34%) than those of the RQQs, ULIRGs, or SDSS ellipticals. They are also significantly larger than those of any other parameters examined in this paper. Such large errors may affect the KS tests. A set of 10,000 Monte Carlo simulations were performed in which a new value of  $\sigma_{\text{o}}$  was randomly generated from within the range of  $\sigma_{\text{o}} \pm \Delta\sigma_{\text{o}}$  for each RLQ. The KS test was then re-run for each Monte Carlo simulation to check for changes in the re-

<sup>12</sup> Equation 7 in Paper I was computed using a least-squares fit with errors in Y array. We have recomputed the fit using **FITEXY**, which produces  $\sigma_{\text{Frac}} = 0.18^{\pm 0.01} \text{Log } L_{\text{IR}} - 1.78^{\pm 0.12}$

sults<sup>13</sup>. As an aid to the reader, the results of all KS tests (1D and 2D) are summarized in Appendix C in Table C1. The values in parentheses in Table C1 show the percentage for which the results remain the same in the simulations compared to the actual test result. Second, although IRAS 19542+1110 is a  $3.9\sigma$  outlier on the FP, excluding it from the KS tests does not change the results presented here and throughout Sections 5.2.1 and 5.2.2.

The Null Hypothesis *cannot* be rejected when the ULIRGs are compared with: the 6 RLQs and all 8 of the QSO host galaxies (RLQs and RQQs). The Null Hypothesis *can* be rejected when the ULIRGs are compared with the *entire* distribution of the SDSS sample. When the comparison is restricted to the SDSS ellipticals in the two largest bins,  $165\text{--}225\text{ km s}^{-1}$  and  $225\text{--}420\text{ km s}^{-1}$ , the Null Hypothesis cannot be rejected for either bin.

We now compare the velocity dispersions of the samples and defer comparisons for  $\log R_{\text{eff}}$  and  $\langle\mu_I\rangle$  to Section 5.2.4 where the RLQ and RQQ samples are significantly larger. A standard (1D) two-sided KS test comparison was made for  $\sigma_o$  between the ULIRGs and QSOs, and the ULIRGs and SDSS ellipticals. It should be noted that the methodology for the standard two-sided KS test uses the tables for small samples or equations for large samples originally published in Pearson & Hartley (1972) as well as the modified KS test which is routinely used in programming language libraries and statistical software (e.g. Fortran, C, C++, IDL, Python, R) for comparisons among samples of any size without the need for comprehensive tables (Stephens 1970; Press et al. 1992). If the two methods disagree, it will be noted, otherwise it is assumed that both methods yield the same result.

The Null Hypothesis can be rejected when the distributions of  $\sigma_o$  are compared for the ULIRGs and RLQs, but only 26% of the time. The Null Hypothesis cannot be rejected when the ULIRGs are compared with all 8 QSO host galaxies (6 RLQs + 2 RQQs). The Null hypothesis can be rejected (and at the 99% level) when comparing the distributions of  $\sigma_o$  for the ULIRGs and the entire SDSS comparison sample.

Figure 3 and the 2D KS tests show that at  $I$ -band ULIRGs lie on the FP in a region where  $M \gg m^*$  ellipticals are found. This is in contrast to pure near-IR studies which showed ULIRGs are systematically offset from the FP in regions dominated by low to intermediate mass ellipticals ( $M \leq m^*$ ) and therefore could not be the progenitors of QSO host galaxies (e.g. Shier & Fischer 1998; Genzel et al. 2001; Tacconi et al. 2002; Dasyra et al. 2006). The comparison with QSO host galaxies is less clear. The  $\sigma_o$  distribution may not be consistent with that of RLQs. The uncertainty arises from the large errors associated with values of  $\sigma_o$  for the RLQs. However, one cannot rule out similarities between ULIRGs and the QSO host galaxy population as a whole.

### 5.2.2. Dynamical Masses & Stellar Populations at $I$ -band

Paper I demonstrated that the *observed* dynamical properties of LIRGs are different at  $I$ -band and  $K$ -band,

an effect not seen in elliptical galaxies. It showed that for a given LIRG, the presence of a central, relatively young population of RSG and/or AGB stars dominates the  $K$ -band light. As a result,  $M_{\text{Dyn}}$  measured at  $K$ -band is significantly smaller than  $M_{\text{Dyn}}$  measured at  $I$ -band. The apparent effective ages also typically younger at  $K$ -band (see Figure 9 in Paper I). At  $I$ -band, this population is largely obscured due to dust, permitting the kinematics of the older, more global population to dominate the observations. Figure 4 is similar to Figure 9 in Paper I. It shows  $M_{\text{Dyn}}$  vs  $M/L$  at  $I$ -band. The ULIRGs, RLQs, RQQs, and SDSS ellipticals are plotted in Figure 4 (same symbols as Figure 3).  $L$  represents the total luminosity and the masses shown are the *total virial*  $M_{\text{Dyn}}$  of each galaxy:

$$M_{\text{Dyn}} = \kappa \frac{\sigma_o^2 R_{\text{eff}}}{G} \quad (5)$$

(Proeda 1958; Fish 1964; Rood et al. 1972; Tonry & Davis 1981; Binney 1982; Bacon et al. 1985; Richstone & Tremaine 1986; Mathews 1988; Bender et al. 1989) where  $R_{\text{eff}}$  is the effective radius from the de Vaucouleurs fit,  $G$  is the gravitational constant, and  $\kappa = 6$  (which takes into account the variations in shape, size, and inclination of spheroids; the impact of rotation on  $\sigma_o$ ; and that  $\sigma$  varies with radius). The values for  $M_{\text{Dyn}}$  are listed in Table 3 for the ULIRGs and Table B2 for the QSO host galaxies. The vertical dotted line represents an  $m^*$  elliptical galaxy. Overlaid are two sets of models representing the evolution of  $M/L$  for a single stellar population (SSP). The pair of models on the left are from (Maraston 2005, hereafter M05). The solid vector is an SSP with solar metallicity and a Kroupa initial mass function (IMF). Changing from solar to either half or twice solar metallicity causes only a slight shift ( $< 0.1$  dex) up or down in  $M/L$ , respectively. The vector shown in light grey parallel to the Kroupa vector is an SSP with solar metallicity and a Salpeter IMF. On the right are updated SSP models from (Bruzual & Charlot 2003, the models are hereafter referred to as CB07). The solid vector is an SSP with solar metallicity and Chabrier IMF and the light grey vector parallel to it is an SSP with solar metallicity and Salpeter IMF. Using sub-solar ( $0.4 Z_{\odot}$ ) or more than solar ( $1.5 Z_{\odot}$ ) metallicity decreases or increases the  $M/L$  values by no more than 0.15 dex. The M05 and CB07 models generally agree with each other at  $I$ -band, although the latter shows more variation/degeneracy in  $M/L$  at  $t \sim 1\text{--}1.2$  Gyr, while M05 shows some variation/degeneracy at  $0.2\text{--}0.4$  Gyr. These are likely related to differences in their treatment of thermally pulsing asymptotic giant branch (TP-AGB) stars (e.g. see M05, Maraston et al. 2006; Bruzual 2007, 2010). Such differences have a more pronounced impact on the analysis of the stellar populations of (U)LIRGs at near-IR wavelengths (e.g. Rothberg 2009; Rothberg & Fischer 2010a, and Paper I) The horizontal placement of both vectors are for display purposes only.

Figure 4 demonstrates that at  $I$ -band, all of the ULIRGs have  $M_{\text{Dyn}} > m^*$ . With the exception of IRAS 19542+1110, the ULIRGs lie at the upper end of the mass distribution. As noted earlier, ULIRGs are known to contain massive quantities of  $\text{H}_2$  and have

<sup>13</sup> The same Monte Carlo tests applied to the other parameters and applied to the errors in  $\sigma_o$  for the ULIRGs and SDSS ellipticals yielded no change in the KS 1D and 2D test results

prodigious star-formation rates. Various methods for estimating the SFR (e.g. Kennicutt 1998; Yun et al. 2001) indicate the 8 ULIRGs plotted in Figure 4 have SFRs  $\sim 100\text{--}500 M_{\odot} \text{ yr}^{-1}$ . Yet, when the  $M/L_I$  values are compared with the SSPs, the stellar populations appear to be old and evolved for 7/8 ULIRGs. A 2D KS test comparison of the distribution of the ULIRGs with the galaxies in the  $I$ -band  $M_{\text{Dyn}}\text{--}M/L$  plane indicates that the Null Hypothesis can be rejected when the ULIRGs are compared with the QSO host galaxies (either the RLQs alone or all 8 QSOs). However, the large RLQ  $\sigma_0$  errors weaken this result significantly, especially when the entire QSO sample is considered (see Table C1 for details). In addition, the Null Hypothesis can be rejected for the *entire* comparison sample of SDSS ellipticals, although the Null Hypothesis cannot be rejected when the ULIRGs are compared with the SDSS ellipticals in the  $165\text{--}225 \text{ km s}^{-1}$  and  $225\text{--}420 \text{ km s}^{-1}$  bins.

It should be noted that Figure 4 presents a simplistic approximation by assuming a single burst population is representative of the entire galaxy, i.e. all stars are of the same age. Moreover, the  $M/L_I$  models shown in Figure 4 are for stellar masses only, whereas the plotted data are dynamical masses. Although SSP models may be an adequate approximation for a typical quiescent elliptical galaxy, the models do not take into account the presence of non-stellar matter (e.g. gas, dust, etc), nor multiple stellar populations (such as a younger population unseen at  $I$ -band, as we posit for LIRGs and ULIRGs). Both the additional ISM mass and the effects of extinction of the  $I$ -band flux from dust will increase the plotted values of  $M/L$ . Thus, the dynamical  $M/L$  is almost always greater than  $M/L$  derived from stellar population models, and in the case of younger galaxies, the inclusion of two populations brings the models more in line with the data (e.g. Gerhard et al. 2001; Cappellari et al. 2006; de Jong & Bell 2007). However, the main point we make here is that at  $I$ -band the ULIRGs appear closer in mass and age to older gEs (with masses well above  $m^*$ ) in contrast to results obtained for the same ULIRGs at near-IR wavelengths. We do not attempt to derive absolute stellar population ages for the ULIRGs using a single bandpass, we simply point out that the comparisons in Figure 4 appear to indicate little or no evidence for the presence of young stars at  $I$ -band, even though they are clearly present at other wavelengths.

Separating the two parameters in Figure 4, we now focus exclusively on  $M_{\text{Dyn}}$  using a standard two-sided KS test. First, for the QSOs, the Null Hypothesis can be rejected (and at the 99% level) when the  $M_{\text{Dyn}}$  distributions of the ULIRGs are compared with the RLQs. Monte Carlo simulations show little change, except at the 99% level. The Null Hypothesis cannot be rejected when the  $M_{\text{Dyn}}$  distributions of the ULIRGs are compared with the entire sample of QSO hosts. Next, the Null Hypothesis can be rejected (and at the 99% level) when the ULIRGs are compared with the entire sample of SDSS ellipticals. The only qualification is that the Null Hypothesis cannot be rejected for the largest  $\sigma_0$  bin. What these results show is that at  $I$ -band the ULIRGs are consistent with gEs possibly including RQQ host galaxies. They may not be consistent with RLQ

host galaxies, but some doubts remain.

### 5.2.3. The Dynamical Masses & Stellar Populations of ULIRGs: Optical vs. Near-IR

As noted earlier, previous dynamical studies of ULIRGs carried out almost exclusively in the near-IR had concluded that for these systems  $M_{\text{Dyn}} \leq m^*$ . Figure 5 demonstrates how the  $\sigma$ -Discrepancy in Section 5.1 can account for the differences between the results in Sections 5.2.1 and 5.2.2 and earlier near-IR only studies. This figure presents a relative comparison of where ULIRGs lie in the  $M_{\text{Dyn}}\text{--}M/L$  plane at  $I$ -band (*top*) and at  $F160W$  ( $\sim H$ -band, *bottom*). Only the ULIRGs which have kinematic and photometric observations at both wavelengths are shown. The ULIRGs are represented by letters in Figure 5, each letter corresponding to a specific galaxy (see the caption for Figure 5 and Table 4). The two plots share the x-axis ( $M_{\text{Dyn}}$ ) in order to enable a direct comparison of the mass computed at both wavelengths. The  $F160W$  photometry and kinematic data from the near-IR CO band-heads are presented in Table 4. As in Figure 4, SSP models from M05 are shown with Kroupa (solid vector) and Salpeter (light grey) solar metallicity IMFs on the left and CB07 for a Chabrier (solid) and Salpeter (light grey) IMFs on the right. The SSP vectors plotted in the  $F160W$  panel were transformed from the original M05 Johnson  $H$ -band values to  $F160W$  using  $(H - F160W)$  colors computed by processing the grid of M05 SEDs at each age with SYNPHOT. At  $F160W$ , the discrepancy between the M05 and CB07 models are more pronounced than at  $I$ -band, particularly for the M05 Kroupa IMF and the CB07 Chabrier and Salpeter IMFs. The relative ages appear to be offset by  $\sim 0.5$  dex between the M05 and CB07. However, regardless of the specific age, ULIRGs clearly appear to be older and more massive at  $I$ -band than at  $F160W$ . As first noted in Paper I, this effect is not seen in elliptical galaxies because they do not have a young stellar population that dominates observations in any wavelength.

### 5.2.4. The Kormendy Relation

The analysis presented above is limited by the number of QSO host galaxies with  $\sigma_0$  measurements, particularly RQQs. The  $\langle \mu \rangle_{\text{eff}}\text{--}\log R_{\text{eff}}$  plane (also known as the Kormendy Relation) is a photometric projection of the FP for early-type systems (e.g. Kormendy 1977, 1982), and, like the FP, is independent of galaxy environment (e.g., Pahre et al. 1998b; Reda et al. 2004; Nigoche-Netro et al. 2007). Although the Kormendy Relation (KR) has significantly more scatter than the FP, it is often used as a “cost-effective” proxy because the stellar absorption line spectroscopy needed to measure  $\sigma_0$  can be time-consuming and/or difficult to obtain. This is especially true for QSOs because observations must contend with the effects of the bright nucleus which can swamp the underlying host galaxy. Until recently, nearly all studies investigating the dynamical properties of QSO host galaxies and their relationship to ellipticals, spirals, and mergers have relied solely on photometric observations. Here, the KR is used to increase the number of QSO host galaxies for comparison from 6 to 28 RLQs, and from 2 to 25 RQQs. The main goals of this section are: 1) to ascertain the positions of advanced ULIRGs with respect to the KR; and 2) to determine where the

ULIRGs lie relative to the elliptical QSO host galaxies.

Figure 6a (*left*) shows the  $I$ -band KR (solid line) derived from the entire comparison sample of SDSS ellipticals using the DWLSQ fitting method described earlier. The derived  $I$ -band KR is:

$$<\mu_1>_{\text{eff}} = 17.52^{\pm 0.01} + 2.26^{\pm 0.01} \text{Log } R_{\text{eff}}. \quad (6)$$

with  $r.m.s. = 0.39$  dex (in units of mag arcsec $^{-1}$ ) and a Pearson Correlation Coefficient of  $r = 0.71$ . This is similar to the fit from Nigoche-Netro et al. (2008) for 8,664 early type galaxies at SDSS  $i$ -band ( $z \leq 0.36$ ). Their slope and intercept is  $2.52^{\pm 0.01}$  and  $17.84^{\pm 0.01}$ , respectively (transformed to  $F814W$ , the intercept is 17.25), with  $r.m.s. = 0.42$  dex and a Pearson Correlation Coefficient of  $r = 0.72$ .

The ULIRGs, RLQs, RQQs, and SDSS ellipticals are plotted in the *left* panel of Figure 6a (same symbols as Figure 3). The diagonal dotted shows the locus of an  $L^*$  galaxy (Blanton et al. 2003; Bell et al. 2003; Hill et al. 2010). Also shown are the 1, 2, and  $3\sigma$  dispersions of the KR (dotted grey lines). As in Figure 3, the SDSS ellipticals follow a gradient in their distribution when grouped by  $\sigma_0$ . The SDSS ellipticals with the largest  $\sigma_0$  lie almost exclusively above the KR and the ones with the smallest  $\sigma_0$  lie almost exclusively below it. In addition to fitting a KR to the entire SDSS comparison sample, fits have been made for each of the SDSS sub-samples (binned by  $\sigma_0$ ) as well as the ULIRGs and QSO host galaxies. The number of objects in each sample, the coefficients of the fit,  $r.m.s.$  and Pearson Correlation Coefficient are provided for each sample in Table 5. The slope of the KR does not vary significantly among the first three  $\sigma_0$  bins, but does decrease significantly for the bin with the highest  $\sigma_0$ . This is somewhat different than the results from Nigoche-Netro et al. (2008), which found that the slope of the KR changes significantly as a function of luminosity when binned in 1 mag intervals and in intervals of increasing luminosity.

The  $r.m.s.$  of the 8 ULIRGs is 1.01, within  $2.5\sigma$  of the KR. However, IRAS 19542+1110 is a significant outlier from the  $I$ -band KR ( $\sim 6\sigma$ ). Excluding it, the  $r.m.s.$  of the ULIRGs decreases to 0.52 ( $\sim 1.3\sigma$  from the KR). Once again, a 2D KS test was used to compare the distribution of the ULIRGs with all of the SDSS ellipticals. Here, the results do change when IRAS 19542+1110 is included or excluded. When included, the Null Hypothesis cannot be rejected. When it is excluded, the Null Hypothesis can be rejected at the 95% level. However, when the ULIRGs are compared with the SDSS ellipticals in the 165-225 km s $^{-1}$  and 225-420 km s $^{-1}$  bins, then the Null Hypothesis cannot be rejected, whether or not IRAS 19542+1110 is excluded. This implies that the ULIRGs are always consistent with the most massive SDSS ellipticals, and the inclusion of IRAS 19542+1110 also makes them consistent with a broader range of ellipticals.

When the ULIRGs are compared with the RLQs, RQQs, and the QSO host galaxies taken together as one sample, the 2D KS test shows that in all cases the Null Hypothesis cannot be rejected. Although the majority of ULIRGs and QSOs fall within  $3\sigma$  of the KR, they lie systematically above the relation. The computed slopes and intercepts are listed in Table 5. Figure 6b (*right*

*panel*) shows the best-fit KRs for the ULIRGs, RLQs, and RQQs from Table 5. The fits are plotted as shaded regions which account for the  $1\sigma$  errors in both slope and intercept.

The ULIRG and QSO fits have steeper slopes than the SDSS ellipticals (including the sub-samples binned by  $\sigma_0$ ). The fits to the ULIRGs and QSOs are consistent with each other. Figure 6b shows the considerable overlap in KR parameter space among ULIRGs, RLQs, and RQQs. Similarly, Veilleux et al. (2009) found at  $F160W$  that the slope of the KR fits to  $PSF$ -subtracted PG QSOs and ULIRGs (in which the bulk of the star-formation should have been removed in the  $PSF$ -subtraction), along with QSOs from D03 and Hamilton et al. (2008), transformed assuming  $(R - H) = 2.8$ , were indistinguishable from each other, but still significantly steeper than inactive ellipticals. The QSO results in Table 5 and Figure 6b also match results from earlier attempts to place QSO host galaxies on the KR at optical wavelengths (e.g. O'Dowd et al. 2002, D03,F04, see bottom of Table 5).

A standard two-sided KS comparison of each individual parameter in the KR ( $<\mu>_{\text{eff}}$  and  $\text{Log } R_{\text{eff}}$ ) between the ULIRGs and the RLQs, RQQs, and the two QSO samples together produces the same result in all cases: the Null Hypothesis cannot be rejected. Given that the ULIRGs are now compared with much larger samples of RLQs and RQQs, Figure 6 presents stronger support than the FP or  $M_{\text{Dyn}}-M/L$  plane for the assertion that ULIRGs are consistent with the host galaxies of QSOs, both as a single population, and when divided into RLQs and RQQs.

Finally, since the RLQ and RQQ photometric samples are sufficiently large, one can compare them with each other using both the 2D KS test and the 1D comparison for each parameter in the KR. Here, the results are quite interesting because the Null Hypothesis cannot be rejected for the 2D case nor can it be rejected for  $<\mu>_{\text{eff}}$ . However, for  $\text{Log } R_{\text{eff}}$  the comparison is less clear. Using the modified KS test, the Null Hypothesis can be rejected at the 95% level, but using the standard KS formula for large samples it cannot be rejected. Such a difference between the methods suggests one should err on the side of caution in making any strong statements about whether the RLQs and RQQs are significantly different in a statistical sense. Both D03 and F04 reached a similar conclusion, noting that the mean  $R_{\text{eff}}$  of RLQs and RQQs are the same within the  $1\sigma$  errors. These results raise doubt about the intrinsic differences between RLQs and RQQs. This reinforces the need for more kinematic ( $\sigma_0$ ) measurements for RLQs and RQQs.

## 6. DISCUSSION

The goal of this paper has been to use the first results of the  $I$ -band dynamical survey of advanced ULIRGs to address two key questions: 1) Does the  $\sigma$ -Discrepancy extend to the more luminous ULIRG population? and 2) At  $I$ -band are the dynamical properties of advanced ULIRGs consistent with gEs, including the host galaxies of QSOs? Here, we briefly discuss the implications for the results presented so far.

### 6.1. The $\sigma$ -Discrepancy

The  $\sigma$ -Discrepancy does appear to extend to ULIRGs such that  $\sigma_{0,\text{CaT}} > \sigma_{0,\text{CO}}$ . Moreover, the results here

agree with what was posited in Paper I, namely the correlation between  $\text{Log } L_{\text{IR}}$  and the  $\sigma$ -Discrepancy, and in turn, the predicted range of  $\sigma_{\text{o,CaT}}$  values for ULIRGs. Just as with the LIRGs in Paper I, the ULIRGs can be described as Janus-like. Like the Roman deity, they present two different faces depending on how they are viewed. At  $I$ -band the face of an old stellar population is observed, while at near-infrared wavelengths the face of a young stellar population dominates (see Figure 19 in Paper I). Since in Paper I, and in this work, we are observing *only* single nuclei mergers, the luminosity evolution of the disks in these systems may be nearly monotonic and decreasing. In this subclass of (U)LIRGs, the lower the  $L_{\text{IR}}$ , the further along will be important processes such as feedback that clears out the star-forming ISM (e.g. Fischer et al. 2010; Feruglio et al. 2010; Sturm et al. 2011) and the subsequent aging of the starburst. As the YCSD becomes fainter, its dominance in both photometric and kinematic measurements in the near-IR subsides, reducing the observed  $\sigma$ -Discrepancy. As the lack of this discrepancy in bonafide ellipticals demonstrates (Paper I, Vanderbeke et al. 2011) at some point in the evolutionary sequence  $\sigma_{\text{o,optical}} = \sigma_{\text{o,near-IR}}$ . Part of this explanation is an oversimplification because it assumes that every merger reaches a ULIRG stage and that LIRGs are stages before and after the luminosity peak. On the other hand, regardless of whether all LIRG mergers will be or at some point have been ULIRGs, lower  $L_{\text{IR}}$  means a less luminous YCSD, and a less dusty nuclear region.

## 6.2. The Evolution of ULIRGs into QSOs

The extension of the  $\sigma$ -Discrepancy to ULIRGs leads directly to the second question; whether the structure and kinematics of ULIRGs are consistent with those of gEs, including QSO host galaxies. We address this in two steps, beginning with a comparison to elliptical galaxies in general. Previous results from near-IR stellar kinematics and photometry (e.g. Genzel et al. 2001; Tacconi et al. 2002; Davies et al. 2004; Colina et al. 2005; Dasyra et al. 2006) concluded ULIRGs were the progenitors of low-intermediate mass ellipticals ( $< m^*$ ) based on two arguments. The first was simply that the measured values of  $\sigma_{\text{o}}$  obtained from near-IR stellar lines were significantly smaller than those of typical or giant ellipticals obtained from optical stellar absorption lines (e.g. Ca H&K, Mg Ib, CaT). This was based on the assumption that the near-IR stellar absorption lines or stellar band-heads probe the global properties of the ULIRGs. The results presented here and in Paper I imply this is not the case. The second is comparing the values of  $M_{\text{Dyn}}$ , computed from the CO  $\sigma_{\text{o}}$  and near-IR photometry, with some fiducial stellar mass representative of the stellar mass function of galaxies. The earlier studies above all used  $m^* = 7.07 \times 10^{10} h^{-2} M_{\odot}$  (or  $1.25 \times 10^{11} M_{\odot}$  for the cosmology used here) from Cole et al. (2001). In other words, because in the near-IR  $M_{\text{Dyn}} < m^*$ , ULIRGs cannot form gEs, let alone an average elliptical. They must be the progenitors of low-intermediate mass ellipticals. However, the value of  $m^*$  used for comparison is actually the larger of two possible values from Cole et al. (2001). The other is  $m^* = 3.43 \times 10^{10} h^{-2} M_{\odot}$  ( $6.0 \times 10^{10} M_{\odot}$  for the cosmology used here). The larger value comes from using a Salpeter

IMF which over-predicts the amount of low-mass stars, rather than a Kennicutt or “diet” Salpeter IMF which compensates for this effect (see Section 6.1 of Bell et al. 2003; Bell & de Jong 2001). A variety of methods have converged towards  $m^* \sim 3 \times 10^{10} M_{\odot}$  (the value used here) which also appears to be the transition region between the blue cloud and red sequence and the threshold above which AGN activity is more likely to be found (e.g. Bell & de Jong 2001; Bell et al. 2003; Kauffmann et al. 2003; Baldry et al. 2004; Bell et al. 2007; Baldry et al. 2008). In other words, the claim that (U)LIRGs form sub- $m^*$  ellipticals is partly based on the selection of the larger of two possible  $m^*$  values. In the bottom panel of Figure 5 the ULIRGs straddle the  $m^*$  line. This remains the same when near-IR data for other advanced ULIRGs from Genzel et al. (2001); Tacconi et al. (2002); Dasyra et al. (2006) are considered. Instead, the real question raised by these earlier results is why the observed  $\sigma_{\text{o,CO}}$  of ULIRGs and near-IR half-light radii were inconsistent with observations at other wavelengths, including molecular gas masses, star-formation rates, high-velocity outflows, etc. Similar to the results for non-IR luminous mergers and LIRGs (e.g. RJ06a, Paper I), the kinematic and photometric properties of the ULIRGs measured at  $I$ -band are now statistically consistent with  $m^*$  and larger ellipticals, including gEs.

QSOs and ULIRGs have a great number of similarities, including: bolometric luminosities and space densities out at least  $z \sim 0.4$  (Soifer et al. 1986; Canalizo & Stockton 2001); an overlap in the FIR-radio correlation (e.g. Sanders & Mirabel 1996; Yun et al. 2001);  $\text{H}_2$  masses of  $\sim 10^9\text{--}10^{10} M_{\odot}$  (e.g. Sanders et al. 1989b; Chini et al. 1997; Evans et al. 2001; Scoville et al. 2003; Bertram et al. 2007; Evans 2009; Evans et al. 2009; Xia et al. 2012); post-starburst stellar populations in or near the nucleus along with tidal tails and peculiar morphologies indicative of a relatively recent gas-rich merging event (e.g. MacKenty & Stockton 1984; Heckman et al. 1986; Hutchings & Neff 1988, 1992; Guyon et al. 2006; Canalizo et al. 2007; Bennert et al. 2008; Ramos Almeida et al. 2011; Tadhunter et al. 2011); and an overlap in the distribution of  $L_{\text{IR}}$  ( $12.24 \pm 0.44$ ,  $12.25 \pm 0.47$ , and  $12.17 \pm 0.16$  for RLQs, RQQs, and ULIRGs, respectively), in which the Null Hypothesis cannot be rejected. However, the sizes and masses of ULIRGs and QSO host galaxies have previously been reported as significantly different. The  $I$ -band dynamical results presented here alleviate this discrepancy. There is now a much stronger dynamical link between ULIRGs and QSO host galaxies. The strongest result comes from the KR, in part, due to the large sample size of QSOs. The 2D KS test for the distribution of objects in the  $\text{Log } R_{\text{eff}}\text{--}\langle\mu_I\rangle_{\text{eff}}$  plane, as well as the two-sided KS tests for each parameter rule out statistical differences between ULIRGs and QSOs (whether grouped together or compared separately as RLQs and RQQs). While past comparisons have relied on the KR to reject the notion that ULIRGs evolve into QSO host galaxies, the same comparison here at  $I$ -band strongly supports the S88 paradigm.

However, it is still important to compare the kinematics of ULIRGs and QSOs. Unfortunately, the tradeoff for doing so is the significantly smaller sample size of

QSOs, including the loss of comparing ULIRGs with only RQQs. The results for the FP are consistent with those of the KR. QSOs (either taken together or just RLQs) and ULIRGs show no statistical difference in their distribution in FP parameter space. It is only when the parameter  $\sigma_*$  is considered alone that things become less clear. There is a weak statistical difference between RLQs and ULIRGs for this parameter (see Table C1), primarily due to the large RLQ errors. In the case of  $M_{\text{Dyn}}$  the differences are stronger and the RLQ  $\sigma_*$  errors do not affect the results significantly (see Table C1). How can these results be reconciled with those from the KR (and its individual parameters) which uses the larger photometric QSO sample? Is  $\sigma_*$  really different for RLQs and ULIRGs, or does it appear to be different because the 6 RLQs in the kinematic sub-sample happen to be non-representative of the larger RLQ sample? To test this, the 2D and standard two-sided KS tests were re-run for the KR and its parameters between the ULIRGs and the *kinematic* QSO sub-sample only. Just one difference emerges from the results listed in Table C1. The Null Hypothesis *can* be rejected for the Log  $R_{\text{eff}}$  comparison between ULIRGs and the 6 RLQs. This explains the rejection of the Null Hypothesis for  $M_{\text{Dyn}}$  between RLQs and ULIRGs because  $\sigma_*$  and Log  $R_{\text{eff}}$  are used to compute the mass. Although the kinematic results for the RLQs are uncertain, when the QSO hosts are considered as a single population, it suggests kinematic similarities exist between them and ULIRGs. Overall, these results clearly demonstrate the need for more measurements of  $\sigma_*$  in RLQs and RQQs to confirm the results from the KR and probe whether the kinematic differences between RLQs and ULIRGs are real (and if any exist between ULIRGs and RQQs).

Although beyond the scope of this paper, these results also raise a conundrum in regards to whether RQQs and RLQs are dynamically different. The Null Hypothesis can be rejected when their luminosities are compared. This implies that their host masses are different (assuming some  $M/L$  transformation from stellar population models and that the ages of the stellar populations in RLQs and RQQs are the same). However, their 2D distributions in the KR are not statistically different (nor are the two parameters when each is compared separately). Since the KR is a projection of the FP, which in turn is related to the correlation between  $M$  and  $M/L$ , it implies that RLQs and RQQs are *not* dynamically different.

## 7. SUMMARY & FUTURE WORK

The main results of this paper are summarized below.

1) The  $\sigma$ -Discrepancy, first reported in RJ06a and quantified in Paper I for LIRGs is shown to extend to ULIRG luminosities. The  $\sigma_*$  measured from the CaT stellar absorption lines are systematically larger than those obtained from the near-IR CO band-heads. With the addition of ULIRGs the correlation between  $\sigma_{\text{Frac}}$  and Log  $L_{\text{IR}}$  remains unchanged from Paper I. We posit that for the single nuclei (U)LIRGs presented here and in Paper I, this relationship results from feedback processes that cause monotonic aging and dimming of the YCSD population and the clearing out of the dusty, star-forming medium.

2) At  $I$ -band, ULIRGs are nearly an order of magnitude more massive than previously measured in the near-IR, and are consistent with ellipticals ranging from  $m^*$  to gEs. All of the ULIRGs presented here lie closer to the Fundamental Plane and Kormendy Relation than in near-IR studies.

3) At  $I$ -band, the  $M/L$  values of ULIRGs appear to indicate the presence of an old, evolved stellar population, similar to quiescent ellipticals. Yet in the near-IR, ULIRGs reflect much younger populations, matching the well established observations of significant quantities of molecular gas and high rates of SFR.

4) At  $I$ -band ULIRGs are dynamically similar to QSO host galaxies, further supporting the S88 paradigm. ULIRGs are statistically consistent with the positions of both RLQs and RQQs on the Fundamental Plane and Kormendy Relation. This result uses the same methods of comparison which in the past have been used to demonstrate that ULIRGs do not evolve into QSO host galaxies. However, when the ULIRGs are compared with the kinematic sub-sample of RLQs, there is a statistical difference (the Null Hypothesis can be rejected) for  $\sigma_*$ ,  $M_{\text{Dyn}}$ , and Log  $R_{\text{eff}}$ . The impact of this difference is weakened by two caveats; the large errors in  $\sigma_*$  for the RLQs which affects the KS tests (see Table C1;) and the contradiction which arises from the Null Hypothesis not being rejected for ULIRGs and RLQs when the full sample of 28 RLQs are considered. These results demonstrate the need for more  $\sigma_*$  measurements for RLQs (to resolve the contradiction) and RQQs in order to make a viable kinematic comparison with ULIRGs and confirm the results presented here.

5) Finally, an homogenized  $I$ -band sample of RLQ and RQQ host galaxies are presented here which can be used for future dynamical studies. The QSO hosts can be used as either a control sample for further comparisons with IR-luminous systems or as a representative sample itself for future studies of QSO host galaxies.

These are the first results from a much broader survey to establish an accurate mass distribution for ULIRGs and to re-evaluate how these systems fit into the broader picture of the formation and evolution of elliptical galaxies and QSOs. It is clear that more kinematic (stellar  $\sigma_*$ ) observations are needed for RLQ and RQQ host galaxies in order to confirm the results presented here. However, the results presented so far are consistent with both the Toomre Hypothesis and QSO evolution scheme presented in S88. Future work will focus on a multi-wavelength approach which will continue to use optical observations to measure  $M_{\text{Dyn}}$  and near-IR observations to probe the central kpc in ULIRGs. A comparison of central black hole masses ( $M_{\bullet}$ ) will also be made, in order to determine the location of ULIRGs with respect to the  $M_{\bullet}$ - $\sigma$  relation. These will require observations to infer  $M_{\bullet}$  independent of  $\sigma$  or host luminosity. Assessing detailed and accurate properties of local ULIRGs is key to formulating a better understanding of similar systems (e.g. dust obscured galaxies, sub-millimeter galaxies, etc..) at higher redshifts.

Some of this research was performed while B. Rothberg held a National Research Council Associateship Award at the Naval Research Laboratory. Basic research in as-

tronomy at the Naval Research Laboratory is funded by the Office of Naval Research. This work was supported in part by a NASA Keck PI Data Award, administered by the NASA Exoplanet Science Institute. Data presented herein were obtained at the W. M. Keck Observatory from telescope time allocated to the National Aeronautics and Space Administration through the agency's scientific partnership with the California Institute of Technology and the University of California. The Observatory was made possible by the generous financial support of the W. M. Keck Foundation. The authors would like to thank: Drs. Sylvain Veilleux and David Rupke for providing information and help with the flux calibration; Drs. David Floyd and Timothy Hamilton for providing additional information and data; and Drs. Gabriela Canalizo and Scott Dahm for helpful discussions. The authors would also like to thank the anonymous referee for useful and detailed comments which strengthened the paper. This research made use of the OSX Version of SCISOFT assembled by Dr. Nor Pirzkal. This work has made use of the EZGal Model Generator (<http://www.baryons.org/ezgal/>). We would also like to acknowledge the University of Maximegalon's MISPWOSO. This research has made use of the NASA/IPAC Extragalactic Database (NED) which is operated by the Jet Propulsion Laboratory, California Institute of Technology, under contract with the National Aeronautics and Space Administration. This publication makes use of data products from the Wide-field Infrared Survey Explorer, which is a joint project of the University of California, Los Angeles, and the Jet Propulsion Laboratory/California Institute of Technology, funded by the National Aeronautics and Space Administration. This work made use of the Sloan Digital Sky Survey (SDSS). Funding for the SDSS and SDSS-II has been provided by the Alfred P. Sloan Foundation, the Participating Institutions, the National Science Foundation, the U.S. Department of Energy, the National Aeronautics and Space Administration, the Japanese Monbukagakusho, the Max Planck Society, and the Higher Education Funding Council for England. The SDSS Web Site is <http://www.sdss.org/>. The SDSS is managed by the Astrophysical Research Consortium for the Participating Institutions. The Participating Institutions are the American Museum of Natural History, Astrophysical Institute Potsdam, University of Basel, University of Cambridge, Case Western Reserve University, University of Chicago, Drexel University, Fermilab, the Institute for Advanced Study, the Japan Participation Group, Johns Hopkins University, the Joint Institute for Nuclear Astrophysics, the Kavli Institute for Particle Astrophysics and Cosmology, the Korean Scientist Group, the Chinese Academy of Sciences (LAMOST), Los Alamos National Laboratory, the Max-Planck-Institute for Astronomy (MPIA), the Max-Planck-Institute for Astrophysics (MPA), New Mexico State University, Ohio State University, University of Pittsburgh, University of Portsmouth, Princeton University, the United States Naval Observatory, and the University of Washington.

**Table 1**  
ULIRG Galaxy Sample

Galaxy Name	R.A. (J2000)	Dec. (J2000)	$z$	$\log L_{\text{IR}}$ ( $L_{\odot}$ )	$E(B - V)$ (mag)
IRAS F02021-2103	02 04 27	-20 49 41	0.116	12.02 <sup>a,b</sup>	0.020
IRAS 05189-2524	05 21 01	-25 21 45	0.043	12.11 <sup>a</sup>	0.026
IRAS F10378+1108	10 40 29	+10 53 18	0.136	12.26 <sup>a,b</sup>	0.029
IRAS 11387+4116	11 41 22	+40 59 51	0.148	12.03 <sup>b,c,d</sup>	0.015
IRAS 12540+5708	12 56 14	+56 52 25	0.042	12.48 <sup>a</sup>	0.009
IRAS 17208-0014	17 23 21	-00 17 01	0.043	12.34 <sup>a</sup>	0.304
IRAS 19542+1110	19 54 35	+11 19 02	0.064	12.03 <sup>a,b</sup>	0.199
IRAS 23365+3604	23 39 01	+36 21 09	0.064	12.13 <sup>a,b</sup>	0.096

**Note.** — R.A. is in units of hours, minutes, and seconds, and Dec is in units of degrees, arcminutes, and arcseconds.  $L_{\text{IR}}$  is the 8-1000  $\mu\text{m}$  total flux measured from the 12, 25, 60, and 100  $\mu\text{m}$  IRAS passbands. (a) All or some IRAS fluxes from Sanders et al. (2003); (b) 12 $\mu\text{m}$  flux from *WISE*; (c) All or some IRAS fluxes from Moshir & et al. (1990); (d) 22 $\mu\text{m}$  flux from *WISE*.

**Table 2**  
ULIRG Observation Log

Galaxy Name	Imaging Camera/Filter	Imaging Integration Time (sec)	ESI Integration Time (sec)	ESI P.A. (deg)	ESI Slitwidth (arcsec)
IRAS F02021-2103 <sup>a</sup>	<i>HST</i> WFPC2/F814W <sup>c</sup>	800	3600	55.0	1.0
IRAS 05189-2524 <sup>b</sup>	<i>HST</i> ACS/F814W <sup>d</sup>	730	900	0.0	1.0
IRAS F10378+1108 <sup>b</sup>	SDSS/Sloan $z$	54.1	1800	0.0	1.0
IRAS 11387+4116 <sup>b</sup>	SDSS/Sloan $z$	54.1	1800	0.0	1.0
IRAS 12540+5708 <sup>a</sup>	<i>HST</i> ACS/F814W <sup>d</sup>	830	900	45.0	0.75
IRAS 17208-0014 <sup>a</sup>	<i>HST</i> ACS/F814W <sup>d</sup> , NIC2/F160W <sup>e</sup>	720,224	3900	40.0	1.0
IRAS 19542+1110 <sup>a</sup>	<i>HST</i> ACS/F814W <sup>d</sup>	720	3600	0.0	1.0
IRAS 23365+3604 <sup>a</sup>	<i>HST</i> ACS/F814W <sup>d</sup> , NIC2/F160W <sup>f</sup>	750,2496	5400	300.0	1.0

**Note.** — (a) ESI P.I. Rothberg; (b) ESI P.I. Sanders; (c) *HST* Program 6346, P.I. Borne; (d) *HST* Program 10592, P.I. Evans; (e) *HST* Program 7219, P.I. Scoville; (f) *HST* Program 11235, Surace. The WFPC2 observations were centered on the WF3 chip.

**Table 3**  
ULIRG Rest-frame  $I$ -band Properties

Galaxy Name	$M_I$ (mag)	$R_{\text{eff}}$ (kpc)	$\langle \mu_I \rangle_{\text{eff}}$ (mag arcsec <sup>-2</sup> )	CaT $\sigma_{\odot}$ (km s <sup>-1</sup> )	CaT $V_{\odot}$ (km s <sup>-1</sup> )	CaT Template Star	$M_{\text{dyn}}$ ( $\times 10^{11} M_{\odot}$ )
IRAS F02021-2103	-23.61 $\pm$ 0.05	9.51 $\pm$ 0.23	19.84 $\pm$ 0.05	209 <sup>a</sup> $\pm$ 8	34679 $\pm$ 8	G8III HD 35369	5.79 $\pm$ 0.46
IRAS 05189-2524	-22.71 $\pm$ 0.09	2.59 $\pm$ 0.10	17.93 $\pm$ 0.12	265 <sup>a</sup> $\pm$ 7	12869 $\pm$ 7	K0III HD 206067	2.54 $\pm$ 0.15
IRAS F10378+1108	-22.96 $\pm$ 0.10	3.09 $\pm$ 0.14	18.05 $\pm$ 0.23	280 <sup>b</sup> $\pm$ 11	41007 $\pm$ 9	G1III $\alpha$ Sge (HD 185758)	3.38 $\pm$ 0.31
IRAS 11387+4116	-23.01 $\pm$ 0.01	3.22 $\pm$ 0.07	18.09 $\pm$ 0.14	198 <sup>b</sup> $\pm$ 9	44575 $\pm$ 7	M0III $\lambda$ Dra (HD 100029)	1.76 $\pm$ 0.16
IRAS 12540+5708	-23.42 $\pm$ 0.10	5.88 $\pm$ 0.27	18.98 $\pm$ 0.13	346 <sup>c</sup> $\pm$ 9	12584 $\pm$ 10	G5II HD 36079	9.86 $\pm$ 0.68
IRAS 17208-0014	-22.88 $\pm$ 0.11	9.37 $\pm$ 0.50	20.54 $\pm$ 0.12	261 <sup>a</sup> $\pm$ 5	12798 $\pm$ 5	K0III HD 206067	8.90 $\pm$ 0.58
IRAS 19542+1110	-23.52 $\pm$ 0.09	0.77 $\pm$ 0.03	14.43 $\pm$ 0.14	169 <sup>a</sup> $\pm$ 6	18718 $\pm$ 5	G8III HD 35369	0.31 $\pm$ 0.02
IRAS 23365+3604	-23.16 $\pm$ 0.08	4.16 $\pm$ 0.19	18.50 $\pm$ 0.10	221 <sup>a</sup> $\pm$ 6	19310 $\pm$ 5	K1.5III $\alpha$ Boo (HD 124897)	2.83 $\pm$ 0.19

**Note.** — Fluxes are in VEGA magnitudes. The values have also been corrected for Galactic Reddening using dust maps from Schlegel et al. (1998) and scaling from Table 6 in Schlafly & Finkbeiner (2011), assuming  $R_V = 3.1$  (Fitzpatrick 1999). The  $A_{\lambda}$  scaling factors used were:  $A_{F814W}$  (ACS/WFC) = 1.52;  $A_{F814W}$  (WFPC2) = 1.54; and  $A_z = 1.26$ . Circular isophotes were used for the *F814W* photometry. Elliptical isophotes were transformed to equivalent radii for SDSS  $z$ -band photometry on IRAS F10378+1108 and IRAS 11387+4116. (a) Measured in 1.53 kpc diameter aperture; (b) Corrected to 1.53 kpc diameter; (c) Measured 2.08 kpc NW from the nucleus and corrected to a 1.53 kpc diameter.

**Table 4**  
Near-IR ULIRG Properties

Galaxy Name	CO $\sigma_o$ (km s <sup>-1</sup> )	$M_{\text{Dyn}}$ via CO ( $\times 10^{11} M_\odot$ )	$R_{\text{eff}}$ ( $F160W$ ) (kpc)	$M_{160W}$ (mag)
IRAS F02021-2103 (A)	143 $\pm$ 21 <sup>a</sup>	1.09	3.85 <sup>d</sup>	-24.89 <sup>f</sup>
IRAS 05189-2524 (B)	131 $\pm$ 16 <sup>a</sup>	0.11	0.48 <sup>d</sup>	-23.96 <sup>f</sup>
IRAS 12540+5708 (C)	117 $\pm$ 10 <sup>b</sup>	0.20	1.05 <sup>d</sup>	-24.22 <sup>f</sup>
IRAS 17208-0014 (D)	223 $\pm$ 15 <sup>c</sup>	0.94 $\pm$ 0.14	1.36 $\pm$ 0.10 <sup>e</sup>	-24.43 $\pm$ 0.18
IRAS 23365+3604 (E)	143 $\pm$ 15 <sup>c</sup>	0.57 $\pm$ 0.13	2.00 $\pm$ 0.22 <sup>e</sup>	-25.25 $\pm$ 0.41

**Note.** — The letters A-E correspond to objects in Figure 5. Fluxes are in VEGA magnitudes. The values have also been corrected for Galactic Reddening using dust maps from Schlegel et al. (1998) and scaling of  $A_{F160W} = 0.51$ , assuming  $R_V = 3.1$  (Fitzpatrick 1999). All values of  $\sigma_{o,CO}$  have been corrected to a common aperture of 1.53 kpc. Some values in the table do not include errors because they were not available from the source materials. (a) Dasyra et al. (2006), M0III template star used (HD 99817); (b) Tacconi et al. (2002) K5Ib template star used (HD 200576); (c) Genzel et al. (2001) M0III template star used (HD 99817); (d) PSF-subtracted Sérsic fit ( $n = 4$ ) (Veilleux et al. 2006) from elliptical isophotes converted to equivalent radii using ellipticities derived from their Table 2; (e) Photometry measured using circular isophotes. (f) Veilleux et al. (2006). The values of  $\sigma_{o,CO}$  in Column 2 and  $M_{\text{Dyn}}$  values computed in Column 3 are only for comparison purposes with the CaT derived properties in Table 3 and do not represent the global properties of the systems.

**Table 5**  
Kormendy Relation Fits

Sample	$N$	Slope	Intercept	$r.m.s.$	$r$
Rest-frame $I$ -band					
SDSS Ellipticals	9255	$2.26 \pm 0.01$	$17.56 \pm 0.01$	0.35	0.71
SDSS Ellipticals $85 \leq \sigma_o \leq 125 \text{ km s}^{-1}$	1656	$2.76 \pm 0.01$	$17.75 \pm 0.01$	0.38	0.76
SDSS Ellipticals $125 < \sigma_o \leq 165 \text{ km s}^{-1}$	3301	$2.69 \pm 0.01$	$17.33 \pm 0.01$	0.36	0.82
SDSS Ellipticals $165 < \sigma_o \leq 225 \text{ km s}^{-1}$	3524	$2.72 \pm 0.01$	$17.02 \pm 0.01$	0.35	0.85
SDSS Ellipticals $225 < \sigma_o \leq 420 \text{ km s}^{-1}$	774	$2.37 \pm 0.02$	$17.00 \pm 0.01$	0.21	0.87
ULIRGs <sup>a</sup>	8	$4.50 \pm 0.14$	$15.68 \pm 0.09$	0.22	0.98
RLQs <sup>b</sup>	28	$3.51 \pm 0.52$	$15.71 \pm 0.45$	0.54	0.79
RQQs <sup>b</sup>	25	$3.40 \pm 0.44$	$16.11 \pm 0.33$	0.56	0.84
All QSO Host Galaxies <sup>b</sup>	53	$3.25 \pm 0.32$	$16.07 \pm 0.26$	0.57	0.81
Restframe $I$ -band for Previously Published Samples <sup>c</sup>					
RLQs (O'Dowd et al. 2002)	16	$3.81 \pm 0.66^d$	$15.37 \pm 0.59$	0.46	0.83
RLQs (D03)	10	$3.66 \pm 0.47^e$	$15.77 \pm 0.42$	0.23	0.93
RLQs (D03, excluding two outliers <sup>f</sup> )	8	$3.05 \pm 0.30^g$	$16.42 \pm 0.29$	0.12	0.97
RQQs (D03)	9	$3.40 \pm 0.73^h$	$16.43 \pm 0.58$	0.37	0.86
RLQs (F04)	7	$3.68 \pm 0.10^i$	$15.83 \pm 0.08$	0.37	0.94
RQQs (F04)	7	$3.13 \pm 0.20^i$	$15.86 \pm 0.15$	0.45	0.91
RLQs + RQQs Combined (F04)	14	$3.20 \pm 0.07^j$	$16.00 \pm 0.06$	0.48	0.91

**Note.** — As a comparison, the earlier  $B$ -band and  $V$ -band KRs had slopes of 3.02 (Kormendy 1977) and 2.94 (Hamabe & Kormendy 1987), respectively, using the surface brightness *at* the effective radius. Two fits each were made to the RLQ, RQQ, and RLQ+RQQ data to account for the absence of errors in the D03 sample. If errors were available a DWLSQ fit, which takes into account errors in  $X$  and  $Y$ , was used. Otherwise, the data points were equally weighted and a standard least-squares fit was used. The fits plotted in Figure 6 include all data for the ULIRGs, RLQs, and RQQs. (a) IRAS 19542+1110 is considered an outlier because it is  $6.3\sigma$  from the KR plotted in Figure 6, while all other ULIRGs are  $\leq 2\sigma$  from the line. Excluding it changes the fit to:  $\langle \mu \rangle_{\text{eff}} 3.85 \pm 0.19 \times \text{Log } R_{\text{eff}} + 16.19 \pm 0.14$ ,  $r.m.s. = 0.24$  and  $r = 0.96$ ; (b) No errors are available for the D03 sample. The KR was fit using a simplified least-squares fit with equal weighting of errors for the dependent data points. When the D03 data are excluded and a DWLSQ method was used the fits change to: RLQs ( $N = 22$ ):  $\langle \mu \rangle_{\text{eff}} 3.58 \pm 0.07 \times \text{Log } R_{\text{eff}} + 15.66 \pm 0.06$ ,  $r.m.s. = 0.57$  and  $r = 0.81$ ; RQQs ( $N = 20$ ):  $\langle \mu \rangle_{\text{eff}} 3.79 \pm 0.09 \times \text{Log } R_{\text{eff}} + 15.15 \pm 0.06$ ,  $r.m.s. = 0.83$  and  $r = 0.83$ ; All QSOs ( $N = 42$ ):  $\langle \mu \rangle_{\text{eff}} 4.23 \pm 0.05 \times \text{Log } R_{\text{eff}} + 14.85 \pm 0.03$ ,  $r.m.s. = 0.74$  and  $r = 0.82$ ; (c) *All* of the QSOs used to derive the previously published KRs are also part of the QSO Comparison Sample in Appendix B. The previously published fits used the surface brightness *at* the effective radius, not the surface brightness *within* the effective radius ( $\langle \mu \rangle_{\text{eff}}$ ), as used here. The original fits used different cosmologies,  $k$ -corrections, transformations to different rest-frame filters, and different fitting techniques. They have been refit here to provide a clean comparison; (d) Original published restframe  $R$ -band published slope =  $2.75 \pm 1.2$ ; (e) Original published observed  $F675W$ -band published slope =  $3.98 \pm 0.71$ ; (f) PG 1004+130 and OX 169; (g) Original published restframe  $R$ -band published slope =  $3.19 \pm 0.67$ ; (h)  $F675W$ -band published slope =  $2.99 \pm 0.34$ ; (i) RLQ and RQQ samples from F04 were not fit separately; (j) Original published restframe  $V$ -band published slope =  $3.33 \pm 0.7$ .

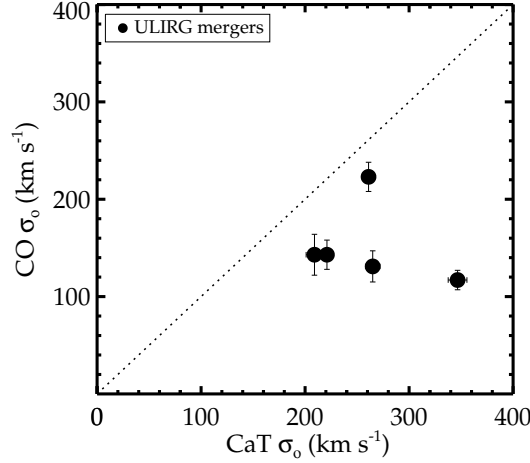


**Figure 1.** Comparison of the central velocity dispersions ( $\sigma_0$ ) measured from the Calcium II Triplet (CaT) stellar absorption lines at  $\lambda \sim 0.85\mu\text{m}$  (x-axis) and those measured from the CO band-head at  $1.6$  or  $2.3\mu\text{m}$  (y-axis) for 5 ULIRGs.

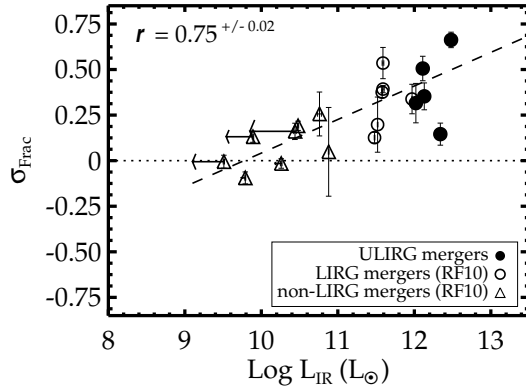


**Figure 2.** Values of  $\sigma_{\text{Frac}}$ , which quantifies the relative difference between  $\sigma_{0,\text{CaT}}$  and  $\sigma_{0,\text{CO}}$  for each advanced merger, are compared with the independently measured quantity  $\text{Log } L_{\text{IR}}$ . The horizontal dotted line represents  $\sigma_{\text{Frac}} = 0$  and the diagonal dashed line shows the weighted least-squares fit to the data. Also shown is the Pearson Correlation Coefficient ( $r$ ). Values of  $r$  range from -1 (strong anti-correlation) to +1 (strong correlation). There is a strong correlation between  $\sigma_{\text{Frac}}$  and  $\text{Log } L_{\text{IR}}$ .

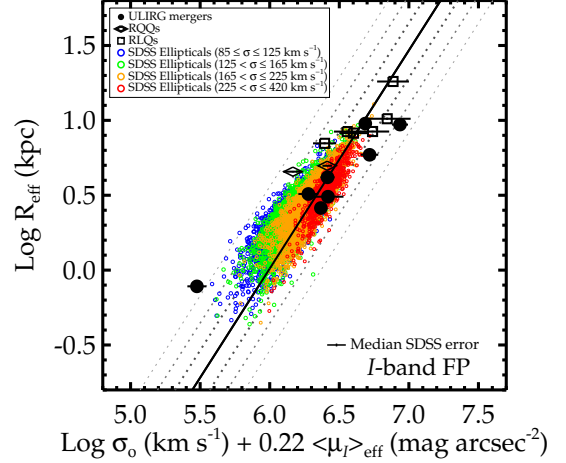


**Figure 3.** The diagonal solid line plotted in this figure represents the  $I$ -band Fundamental Plane (Hyde & Bernardi 2009b) seen edge-on. It is transformed from the Sloan  $i$ -band filter to our preferred cosmology. Plotted in this figure are: advanced ULIRGs (filled circles), the host galaxies of Radio Loud (open squares), and Radio Quiet (open flattened diamonds) QSOs, and the SDSS comparison sample of 9,255 ellipticals (open circles in four colors). In this, and subsequent plots, the SDSS ellipticals are shown binned into four groups based on  $\sigma_0$ : 1)  $85 \text{ km s}^{-1} \leq \sigma_0 \leq 125 \text{ km s}^{-1}$  (1656 blue); 2)  $120 \text{ km s}^{-1} < \sigma_0 \leq 165 \text{ km s}^{-1}$  (3301 green); 3)  $165 \text{ km s}^{-1} < \sigma_0 \leq 225 \text{ km s}^{-1}$  (3524 orange); and 4)  $225 \text{ km s}^{-1} < \sigma_0 \leq 420 \text{ km s}^{-1}$  (774 red). The ULIRGs and QSO host galaxies have values of  $\sigma_0$  which would place them in either the 3rd or 4th bin. Error bars are plotted for the ULIRG sample and QSOs (where available), along with the median errors for the SDSS sample. Over-plotted are the 1, 2, and 3 $\sigma$  scatter of the FP (dotted diagonal lines in dark to light grey).

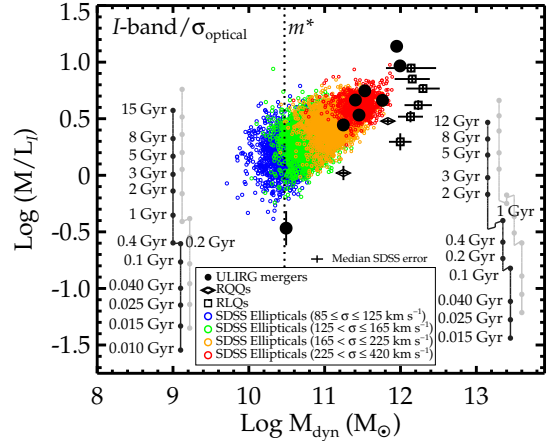


**Figure 4.** This figure compares ( $M_{\text{DYN}}$ ) and  $M/L$  values at  $I$ -band. Plotted here are the ULIRGs, SDSS comparison ellipticals and QSO host galaxies (same symbols used in Figure 3). The over-plotted solid vectors in the panel show the temporal evolution of  $M/L$  for a burst single stellar population (SSP) with solar metallicity and a Kroupa (solid black line) or Salpeter (grey line) IMF (M05). The value of  $M$  for the SSPs represents the stellar mass ( $m^*$ ) while the masses plotted for the galaxies are the total virial dynamical mass ( $M_{\text{DYN}}$ ). The horizontal placement of the  $M/L$  vectors are for display only. The vertical dotted line represents the mass of an  $m^*$  galaxy ( $\sim 3 \times 10^{10} M_{\odot}$ ). Error bars are plotted for the ULIRG sample and QSOs (where available), along with the median errors for the SDSS sample.

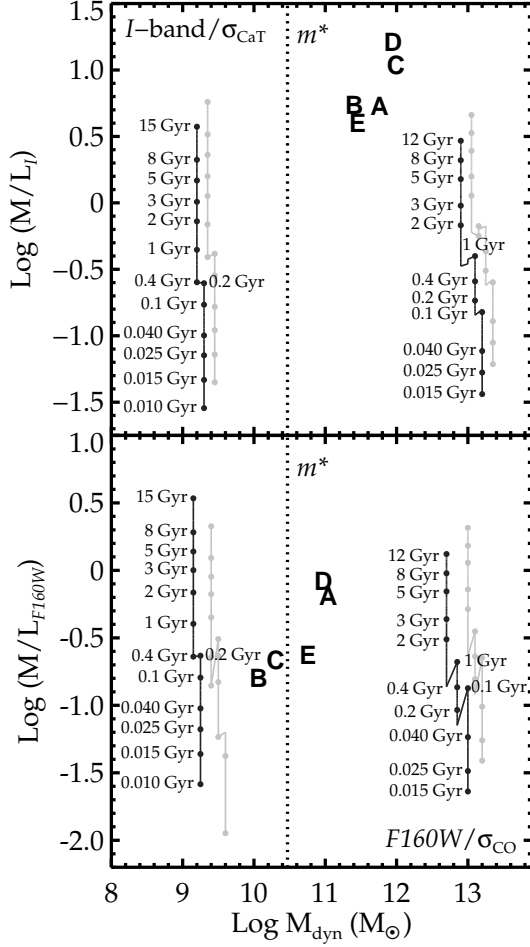


**Figure 5.** Shown here is a plot similar to Figure 4, comparing the same set of ULIRGs at  $I$ -band (*top*) with their parameters at  $F160W$  (*bottom*). The *top* panel uses  $I$ -band photometry along with  $\sigma_{o, CaT}$  and the *bottom* panel uses HST/NIC2  $F160W$  photometry with  $\sigma_{o, CO}$ . The 5 ULIRGs plotted in both panels are: A = IRAS F02021-2103, B = IRAS 05189-2524, C = IRAS 12540+5708, D = IRAS 17208-0014, and E = IRAS 23365+3604. The solid vectors in both panels represent the temporal evolution of  $M/L$  at  $I$ -band (*top*) and  $F160W$  (*bottom*) for a SSP with solar metallicity and a Kroupa (solid black line) or Salpeter (grey line) IMF (M05). Once again, the  $M$  from the SSPs represents the stellar mass ( $m^*$ ), while for the plotted galaxies it represents  $M_{dyn}$ . The horizontal placement of the  $M/L$  vectors in both panels are for display only. The vertical dotted line in both panels represents an  $m^*$  galaxy ( $\sim 3 \times 10^{10} M_{\odot}$ ). In the bottom panel ULIRGs A, B, and C have been  $PSF$ -subtracted (FWHM = 0.14 arcsec pixel $^{-1}$  corresponding to 0.27, 0.11, and 0.10 kpc for A, B, and C, respectively). This has likely removed some of the star-formation contribution to the galaxy luminosity. Therefore, their vertical positions in the bottom panel are upper limits suggesting their ages and  $M/L$  may be smaller than what is shown.

## APPENDIX

### A. SLOAN DIGITAL SKY SURVEY COMPARISON SAMPLE SELECTION CRITERIA

The selection criteria used to generate the SDSS comparison sample are described below. They are based upon the criteria used in Bernardi et al. (2003b); Hyde & Bernardi (2009a,b) to select early-type galaxies

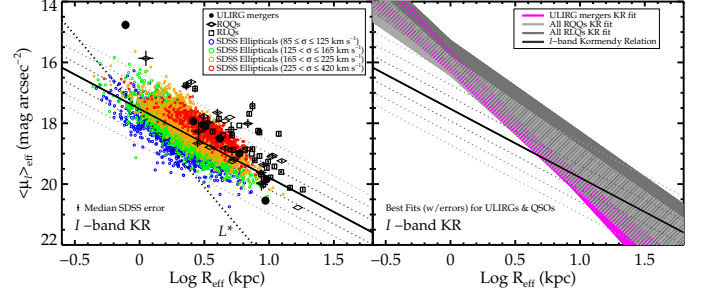


**Figure 6.** Shown in both panels is the Kormendy Relation (KR), a photometric projection of the Fundamental Plane. The *left* panel compares photometric properties of the sample of 8 advanced ULIRGs with a larger sample of 28 RLQ and 25 RQQ host galaxies. The diagonal solid black line plotted in this figure represents the  $I$ -band KR computed from the SDSS comparison sample of 9,255 Ellipticals ( $r.m.s. = 0.39$  dex). Error bars are plotted for the ULIRG sample and QSOs (where available), along with the median errors for the SDSS sample. The diagonal dashed line shows the range of  $\langle \mu_l \rangle$  and  $\text{Log } R_{eff}$  for an  $L^*$  galaxy of constant luminosity. The dotted grey lines (from dark to light) represent 1, 2, and  $3 \times r.m.s.$  of the KR. The  $r.m.s.$  of the various samples are: ULIRGs = 1.01 (0.52 without IRAS 19542+1110), RLQs = 0.95, RQQs = 0.91, all QSOs = 0.93. Plotted in the *right* panel are the derived fits to the ULIRGs, RLQs, and RQQs from Table 5. The filled regions for each sample display the fit including the  $\pm 1\sigma$  errors in the slope and intercept. The diagonal solid black and dotted grey lines represent the KR and the  $1-3 \times r.m.s.$  from the fit.

(including S0 or lenticulars) for deriving the Fundamental Plane in several bandpasses. The criteria are divided into photometric (items 1-7) and spectroscopic (items 8-12) categories. The selection criteria required that the elliptical galaxy must be present in both the photometric (PhotoObjA11) and spectroscopic (SpecObj) databases. Only Sloan  $i$ -band photometry was used for the photometric catalog. No magnitude or flux limitations were imposed on the sample.

The biggest differences between the selection criteria used here and those in Bernardi et al. (2003b); Hyde & Bernardi (2009a,b) are: redshift ( $z \leq 0.15$  here vs. 0.36); restricting the sample to elliptical morphologies only (affected by `ln1Dev` and `ln1Exp`; and  $\sigma \geq 85$  km s $^{-1}$  vs 60 km s $^{-1}$  to avoid the effects of instrumental resolution (see Appendix B in Bernardi et al. (2003b)). No parameters or values for those parameters were selected that would exclude any elliptical in the comparison sample from being a part of the HB09 sample.

1) `MODE` = 1 selects the primary photometry for each object, rejecting possible duplications as well as objects flagged as saturated, near the edge of a CCD.

2) `PARENTID` = 0 and `nCHILD` = 0 rejects galaxies blended with other objects, or the child of a de-blended set of objects. Given the spatial resolution of the photometry and spectral resolution of the data, de-blended superimposed objects may yield unrealistic measured parameters. Not setting these parameters resulted in a number of double counted galaxies in which the same  $\sigma$  is assigned to both parent and child galaxy, producing spurious results.

3) `FRACDEV` = 1: defined as the fraction of total flux which contributes to a de Vaucouleurs (de Vaucouleurs 1953) or  $r^{1/4}$  fit to the galaxy light profile.

4) `devAB`  $\geq 0.6$ : defined as the axis ratio of the minor to major axis for a de Vaucouleurs fit. Analysis

by Hyde & Bernardi (2009a,b) demonstrated that while  $\text{FRACDEV} = 1$  eliminates most disk galaxies from SDSS photometric catalogs, a non-trivial amount remain. Values of  $\text{devAB} \geq 0.6$  significantly improve the removal of late-type galaxies.

5) **Type = 3**: Morphological classification as a galaxy.

6) **lnlExp** & **lnlDev** > -9999: **lnlExp** and **lnlDev** are maximum likelihood functions which estimates the best-fit model parameters convolved with an estimate of the seeing. Smaller values indicate a larger likelihood. The criteria cutoff assure that the measured values have meaning, as values of -9999 mean no data is available.

7) **lnlDev** at least 10% > **lnlExp**: This criteria selects objects in which the likelihood of a de Vaucouleurs fit is 10% greater than an exponential fit. This is a recommended setting from SDSS for selecting elliptical galaxies.

8) **specObjID**  $\neq 0$ : reject objects without spectroscopic observations.

9) **SpecClass** = 2: Spectral classification as a galaxy.

10) **eClass** < 0: a one-dimensional classification of spectral type from Principal Component Analysis (Yip et al. 2004) in which negative values correspond to absorption line galaxies with old stellar populations and positive values correspond to star-forming galaxies.

11) **sn0**, **sn1**, and **sn2**  $\geq 10.0$ : The values of  $\sigma$  in DR7 are measured by fitting the rest-frame wavelength range 0.4-0.7  $\mu\text{m}$ . The **sn0**, **sn1**, and **sn2** criteria were selected to ensure  $\sigma$  was measured from spectra with sufficient S/N.

12)  $\sigma \geq 85 \text{ km s}^{-1}$  and  $< 420 \text{ km s}^{-1}$ : The SDSS spectra are re-sampled to a dispersion of  $\log \lambda = 10^{-4} \text{ dex pixel}^{-1}$  which corresponds to  $69 \text{ km s}^{-1}$ . The actual spectral resolution varies from 85-105  $\text{km s}^{-1}$  for galaxies in the SDSS spectra (Bernardi et al. 2003b) due to variations as a function of wavelength. The DR7 (and DR6)  $\sigma$  values differ from earlier data releases in that they are measured using a direct-fitting method (Rix & White 1992) with the assumption of a Gaussian profile, rather than a Fourier fitting routine. The latter appears to bias  $\sigma$ 's  $< 150 \text{ km s}^{-1}$  systematically higher (Bernardi 2007). The direct-fitting method is the same method used for measuring the  $\sigma_0$  from the spectra of the ULIRGs presented here although the profile shape is fit with a Gauss-Hermite polynomial rather than a Gaussian because the S/N is higher (see Section 3, RJ06a, and Paper I). The DR7 release notes also warn that  $\sigma > 420 \text{ km s}^{-1}$  are not reliable. To err on the side of caution we have selected the lower cutoff to be the approximate limit of, rather than below the instrumental resolution.

Finally, for completeness, we apply a rest-frame radius correction for each elliptical galaxy in the SDSS comparison sample. Since early-type galaxies have color gradients, yielding slightly larger  $R_{\text{eff}}$  at bluer wavelengths, we use equation 6 from Hyde & Bernardi (2009a), which interpolates the observed radii from adjacent bands. The median correction is +0.012 kpc.

## B. DATA FOR THE COMPARISON SAMPLES OF RLQ & RQQ HOST GALAXIES

**Table 1**  
QSO Comparison Sample

Galaxy Name	R.A. (J2000)	Dec. (J2000)	$z$	Log $L_{\text{IR}}$ ( $L_{\odot}$ )	$E(B - V)^a$ (mag)	Camera/ Filter	$M_{\text{I}}$ (mag)	$R_{\text{eff}}$ (kpc)	$\langle \mu_{\text{I}} \rangle_{\text{eff}}$ (mag arcsec $^{-2}$ )
Radio Loud QSO Comparison Sample									
HB89 0031-707	00 34 05	-70 25 52	0.363	12.22 <sup>b,c,d,3,4</sup>	0.031	WF3/ <i>F791W</i> <sup>†</sup>	-23.79 $\pm$ 0.08	7.74 $\pm$ 0.28	19.21 $\pm$ 0.08
HB89 0110+297	01 13 24	+29 58 15	0.363	12.47 <sup>b,c,d,3,4</sup>	0.063	WF2/ <i>F814W</i> <sup>†</sup>	-23.57 $\pm$ 0.14	8.66 $\pm$ 0.56	19.67 $\pm$ 0.12
3C48	01 37 41	+33 09 35	0.367	13.03 <sup>b,1,2,3,4</sup>	0.044	PC/ <i>F814W</i> <sup>*</sup>	-25.59 $\pm$ 0.03	11.85 $\pm$ 0.10	18.34 $\pm$ 0.10
PKS 0137+012	01 39 57	+01 31 46	0.260	12.54 <sup>b,c,3,4</sup>	0.029	WF2/ <i>F675W</i> <sup>*</sup>	-24.26 $\pm$ 0.03	9.81 $\pm$ 0.13	19.26 $\pm$ 0.07
PKS 0202-76	02 02 13	-76 20 03	0.389	12.66 <sup>b,d,3,4</sup>	0.051	PC/ <i>F702W</i> <sup>*</sup>	-23.84 $\pm$ 0.07	2.68 $\pm$ 0.08	16.84 $\pm$ 0.12
3C59	02 07 09	+29 31 41	0.109	(11.75) <sup>b</sup>	0.063	WF2/ <i>F675W</i> <sup>‡</sup>	-23.31	5.28	18.86
PKS 0312-77	03 11 55	-76 51 51	0.223	11.92 <sup>b,c,4</sup>	0.097	PC/ <i>F702W</i> <sup>*</sup>	-24.35 $\pm$ 0.02	10.98 $\pm$ 0.07	19.42 $\pm$ 0.08
PKS 0736+01	07 39 18	+01 37 05	0.191	11.80 <sup>e,4</sup>	0.128	WF2/ <i>F675W</i> <sup>*</sup>	-24.12 $\pm$ 0.02	8.42 $\pm$ 0.09	19.07 $\pm$ 0.06
PKS 0812+02	08 15 22	+01 55 00	0.402	12.44 <sup>b,c,3,4</sup>	0.029	WF2/ <i>F814W</i> <sup>†</sup>	-24.43 $\pm$ 0.03	12.39 $\pm$ 0.21	19.60 $\pm$ 0.05
PKS 0903+16	09 06 31	+16 46 12	0.412	12.83 <sup>b,c,d</sup>	0.040	PC/ <i>F814W</i> <sup>*</sup>	-23.89 $\pm$ 0.24	5.09 $\pm$ 0.55	18.20 $\pm$ 0.25
PG 1004+130	10 07 26	+12 38 56	0.240	12.26 <sup>c,g,4</sup>	0.040	WF2/ <i>F675W</i> <sup>‡</sup>	-24.34	5.88	18.07
PKS 1020-103	10 22 32	-10 37 44	0.190	11.17 <sup>c,d,e</sup>	0.046	WF2/ <i>F675W</i> <sup>‡</sup>	-23.39	4.40	18.39
PKS 1058+110	11 00 47	+10 46 13	0.422	11.41 <sup>c,d,e</sup>	0.026	WF2/ <i>F814W</i> <sup>†</sup>	-23.32 $\pm$ 0.18	9.01 $\pm$ 0.75	20.01 $\pm$ 0.14
HB89 1150+497	11 53 24	+49 31 09	0.333	12.29 <sup>c,d,f,4</sup>	0.021	WF2/ <i>F814W</i> <sup>†</sup>	-23.74 $\pm$ 0.08	5.18 $\pm$ 0.18	18.39 $\pm$ 0.11
HB89 1208+322	12 10 37	+31 57 06	0.389	12.31 <sup>b,c,d,3</sup>	0.017	WF3/ <i>F791W</i> <sup>†</sup>	-23.11 $\pm$ 0.03	3.66 $\pm$ 0.05	18.26 $\pm$ 0.05
PKS 1217+02	12 20 11	+02 03 42	0.240	12.22 <sup>b,d,4</sup>	0.022	WF2/ <i>F675W</i> <sup>‡</sup>	-23.89	7.35	19.00
PG 1226+023	12 29 06	+02 03 09	0.158	12.72 <sup>g</sup>	0.021	WF3/ <i>F606W</i> <sup>*</sup>	-24.89 $\pm$ 0.04	8.41 $\pm$ 0.13	18.29 $\pm$ 0.10
PKS 1233-24	12 35 37	-25 12 17	0.355	12.46 <sup>b,c,d</sup>	0.097	WF2/ <i>F814W</i> <sup>†</sup>	-23.60 $\pm$ 0.07	2.27 $\pm$ 0.07	16.75 $\pm$ 0.05
PG 1302-102	13 05 33	-10 33 19	0.278	12.35 <sup>c,d,h</sup>	0.043	WF3/ <i>F606W</i> <sup>*</sup>	-24.89 $\pm$ 0.04	8.21 $\pm$ 0.15	18.24 $\pm$ 0.10
PG 1425+267	14 27 35	+26 32 14	0.366	12.64 <sup>d,i,3,4</sup>	0.019	WF3/ <i>F814W</i> <sup>*</sup>	-24.25 $\pm$ 0.03	14.50 $\pm$ 0.20	20.12 $\pm$ 0.10
PG 1545+210	15 47 43	+20 52 17	0.264	11.95 <sup>c,g,4</sup>	0.042	WF3/ <i>F606W</i> <sup>*</sup>	-24.06 $\pm$ 0.05	7.42 $\pm$ 0.17	18.85 $\pm$ 0.09
PG 1704+608	17 04 41	+60 44 31	0.372	12.71 <sup>g,4</sup>	0.069	PC/ <i>F702W</i> <sup>*</sup>	-25.48 $\pm$ 0.07	7.43 $\pm$ 0.20	17.43 $\pm$ 0.16
PKS 2135-14	21 37 45	-14 32 56	0.200	12.06 <sup>b,c,d,4</sup>	0.050	WF2/ <i>F675W</i> <sup>*</sup>	-23.84 $\pm$ 0.03	10.25 $\pm$ 0.16	19.78 $\pm$ 0.07
OX 169	21 43 35	+17 43 49	0.211	11.99 <sup>b,c,d,3,4</sup>	0.111	WF2/ <i>F675W</i> <sup>*</sup>	-23.77 $\pm$ 0.03	4.09 $\pm$ 0.02	17.85 $\pm$ 0.13
4C +31.63	22 03 15	+31 45 38	0.295	12.82 <sup>b,c,d,3,4</sup>	0.124	PC/ <i>F702W</i> <sup>*</sup>	-25.11 $\pm$ 0.03	7.02 $\pm$ 0.09	17.68 $\pm$ 0.08
PKS 2247+14	22 50 25	+14 19 52	0.237	12.18 <sup>b,c,3,4</sup>	0.050	WF2/ <i>F675W</i> <sup>*</sup>	-24.01 $\pm$ 0.02	9.59 $\pm$ 0.08	19.46 $\pm$ 0.07
PG 2349-014	23 51 56	-01 09 13	0.174	11.81 <sup>c,d,g</sup>	0.027	WF2/ <i>F675W</i> <sup>*</sup>	-24.68 $\pm$ 0.02	18.18 $\pm$ 0.12	20.18 $\pm$ 0.06
PKS 2355-082	23 58 09	-08 00 04	0.210	11.86 <sup>b,c,d,3,4</sup>	0.040	WF2/ <i>F675W</i> <sup>‡</sup>	-23.76	6.50	18.87
Radio Quiet QSO Comparison Sample									
LBQS 0020+0018	00 23 11	+00 35 18	0.423	12.33 <sup>b,c,d,3</sup>	0.024	PC/ <i>F675W</i> <sup>*</sup>	-23.59 $\pm$ 0.12	2.29 $\pm$ 0.12	16.78 $\pm$ 0.13
HB89 0054+144	00 57 09	+14 46 10	0.171	12.36 <sup>b,d,4</sup>	0.046	WF3/ <i>F606W</i> <sup>*</sup>	-23.92 $\pm$ 0.04	4.54 $\pm$ 0.05	17.92 $\pm$ 0.13
LBQS 0100+0205	01 03 13	+02 21 10	0.393	12.62 <sup>b,c,d,3,4</sup>	0.021	PC/ <i>F675W</i> <sup>*</sup>	-23.23 $\pm$ 0.23	3.35 $\pm$ 0.34	17.96 $\pm$ 0.24
Mrk 1014	01 59 50	+00 23 41	0.164	12.59 <sup>g</sup>	0.029	WF2/ <i>F675W</i> <sup>‡</sup>	-24.56	10.45	19.10
HB89 0244+194	02 47 40	+19 40 58	0.176	11.59 <sup>b,c,d,3,4</sup>	0.110	WF2/ <i>F675W</i> <sup>*</sup>	-23.01 $\pm$ 0.06	5.31 $\pm$ 0.14	19.18 $\pm$ 0.09
HS 0624+6907	06 30 02	+69 05 04	0.370	12.62 <sup>b,c,d,3,4</sup>	0.098	WF3/ <i>F791W</i> <sup>†</sup>	-24.73 $\pm$ 0.16	6.84 $\pm$ 0.49	18.01 $\pm$ 0.15
MS 0754.6+3928	07 58 00	+39 20 39	0.096	11.69 <sup>c,d,j,4</sup>	0.066	PC/ <i>F814W</i> <sup>*</sup>	-23.91 $\pm$ 0.04	2.49 $\pm$ 0.04	16.64 $\pm$ 0.10
PG 0923+201	09 25 54	+19 54 05	0.190	12.07 <sup>c,d,j</sup>	0.042	WF3/ <i>F606W</i> <sup>*</sup>	-23.64 $\pm$ 0.05	8.69 $\pm$ 0.20	19.62 $\pm$ 0.10
PG 0953+415	09 56 52	+41 15 22	0.234	11.82 <sup>c,d</sup>	0.012	WF2/ <i>F675W</i> <sup>‡</sup>	-22.89	5.20	19.25
PG 1001+291	10 04 02	+28 55 35	0.329	12.80 <sup>b,3,4</sup>	0.022	WF3/ <i>F791W</i> <sup>†</sup>	-23.98 $\pm$ 0.08	9.01 $\pm$ 0.35	19.36 $\pm$ 0.10
PG 1012+008	10 14 54	+00 33 37	0.186	11.93 <sup>c,d,3,4</sup>	0.031	WF2/ <i>F675W</i> <sup>‡</sup>	-23.90	16.66	20.77
He 1029-1401	10 31 54	-14 16 51	0.086	11.35 <sup>b,c,4</sup>	0.067	WF3/ <i>F606W</i> <sup>*</sup>	-23.24 $\pm$ 0.02	5.19 $\pm$ 0.04	18.90 $\pm$ 0.08
PG 1202+28	12 04 42	+27 54 12	0.165	11.72 <sup>c,g</sup>	0.021	WF3/ <i>F606W</i> <sup>*</sup>	-23.27 $\pm$ 0.03	3.12 $\pm$ 0.04	17.77 $\pm$ 0.10
PG 1216+069	12 19 20	+06 38 39	0.331	12.53 <sup>c,d,i,3,4</sup>	0.022	PC/ <i>F702W</i> <sup>*</sup>	-23.30 $\pm$ 0.18	8.72 $\pm$ 0.70	19.96 $\pm$ 0.25
LBQS 1230+0947	12 33 25	+09 31 23	0.414	13.02 <sup>b,c,3,4</sup>	0.021	WF3/ <i>F791W</i> <sup>†</sup>	-23.92 $\pm$ 0.08	3.98 $\pm$ 0.13	17.65 $\pm$ 0.13
EQS B1252+0200	12 55 19	+01 44 12	0.345	12.59 <sup>b,d,3,4</sup>	0.018	WF3/ <i>F791W</i> <sup>†</sup>	-22.57 $\pm$ 0.28	2.85 $\pm$ 0.36	18.27 $\pm$ 0.30
EQS B1254+0206	12 57 06	+01 50 39	0.421	12.71 <sup>b,c,3,4</sup>	0.020	WF2/ <i>F814W</i> <sup>†</sup>	-24.64 $\pm$ 0.04	10.62 $\pm$ 0.22	19.05 $\pm$ 0.04
EQS B1255-0143	12 58 15	-01 59 19	0.410	12.39 <sup>b,c,d,3,4</sup>	0.018	WF2/ <i>F814W</i> <sup>†</sup>	-22.94 $\pm$ 0.29	1.11 $\pm$ 0.14	15.86 $\pm$ 0.25
PG 1307+085	13 09 47	+08 19 48	0.155	11.73 <sup>c,d,g,4</sup>	0.033	WF3/ <i>F606W</i> <sup>*</sup>	-23.05 $\pm$ 0.05	4.58 $\pm$ 0.10	18.82 $\pm$ 0.11
PG 1416-129	14 19 03	-13 10 44	0.129	11.49 <sup>c,d,i,3,4</sup>	0.094	PC/ <i>F814W</i> <sup>*</sup>	-22.14 $\pm$ 0.08	2.80 $\pm$ 0.10	18.66 $\pm$ 0.13
PG 1444+407	14 46 45	+40 35 06	0.267	12.43 <sup>c,g</sup>	0.014	WF3/ <i>F606W</i> <sup>*</sup>	-24.24	4.97	17.80
HB89 1549+203	15 52 02	+20 14 02	0.250	12.33 <sup>b,c,d,3,4</sup>	0.054	WF2/ <i>F675W</i> <sup>‡</sup>	-22.49	3.48	18.78
HB89 1635+119	16 37 46	+11 49 49	0.146	11.83 <sup>b,c,d</sup>	0.052	WF2/ <i>F675W</i> <sup>*</sup>	-23.18 $\pm$ 0.02	4.16 $\pm$ 0.03	18.47 $\pm$ 0.06
HB89 1821+643	18 21 57	+64 20 36	0.297	13.05 <sup>c,j</sup>	0.043	WF3/ <i>F791W</i> <sup>†</sup>	-24.81 $\pm$ 0.02	12.52 $\pm$ 0.13	19.23 $\pm$ 0.05
HB89 2215-037	22 17 47	-03 32 38	0.242	12.37 <sup>b,3,4</sup>	0.106	PC/ <i>F702W</i> <sup>*</sup>	-23.88 $\pm$ 0.02	6.79 $\pm$ 0.06	18.84 $\pm$ 0.08

**Note.** — PC = Planetary Camera; WF2 = Wide Field 2; WF3 = Wide Field 3; WF4 = Wide Field 4. All rest-frame  $I$ -band photometry is in Vega magnitudes and has been corrected for Galactic Reddening. The  $A_{\lambda}$  scaling factors used were:  $A_{F606W} = 2.41$ ;  $A_{F675W} = 2.52$ ;  $A_{F702W} = 1.94$ ;  $A_{F791W} = 1.74$ ;  $A_{F814W} = 1.54$ . The  $R_{\text{eff}}$  listed in this table are equivalent radii. (a) Galactic reddening values from (Schlegel et al. 1998); (b) Fluxes from NASA/IPAC Scan Processing and Integration tool; (c) 12 $\mu$ m flux from *WISE*; (d) 22 $\mu$ m flux from *WISE*; (e) computed only from 12 and 22 $\mu$ m *WISE* fluxes; (f) Impey & Neugebauer (1988); (g) Sanders et al. (1989a); (h) Haas et al. (2000) based on ISO photometry; (i) Haas et al. (2003) based on ISO photometry; (j) IRAS Faint Source Catalog; (1) upper limits ( $3 \times r.m.s.$ ) used for  $f_{12}$ ; (2) upper limits ( $3 \times r.m.s.$ ) used for  $f_{25}$ ; (3) upper limits ( $3 \times r.m.s.$ ) used for  $f_{60}$ ; (4) upper limits ( $3 \times r.m.s.$ ) used for  $f_{100}$ . The IRAS fluxes for 3C59 were computed from  $3\sigma$  upper limits only and noted in parentheses above. (†) *HST/WFPC2* Photometry from (Floyd et al. 2004, Floyd, private communication); (\*) *HST/WFPC2* Photometry from (Hamilton et al. 2002, 2008, Hamilton, private communication); (‡) *HST/WFPC2* Photometry from Dunlop et al. (2003). Although  $R$ -band values are listed in the paper, they are actually values for the *F675W* filter and were not transformed to Cousins  $R$ -band; (★) *HST/WFPC2* Photometry from Bahcall et al. (1997).

**Table 2**  
QSO Host Kinematic Properties

Galaxy Name	Optical $\sigma_0$ (km s <sup>-1</sup> )	$M_{\text{dyn}}$ ( $\times 10^{11} M_{\odot}$ )
Radio Loud QSOs		
PKS 0736+01	348 $\pm$ 83	14.28 $\pm$ 7.62
PG 1226+023	339 $\pm$ 58	13.54 $\pm$ 5.15
PG 1302-102	386 $\pm$ 72	17.13 $\pm$ 7.13
PKS 2135-14	310 $\pm$ 106	13.78 $\pm$ 10.50
4C +31.63 <sup>a</sup>	318 $\pm$ 49	9.92 $\pm$ 3.39
PG 2349-014 <sup>a</sup>	279 $\pm$ 64	19.78 $\pm$ 10.09
Radio Quiet QSOs		
HB89 0054+144	167 $\pm$ 11	1.76 $\pm$ 0.26
PG 1444+407	313 $\pm$ 22	6.81 $\pm$ 1.07

**Note.** — All  $\sigma_0$  values are measured using the Ca II H&K stellar absorption line over the 0.385-0.42  $\mu\text{m}$  wavelength range. All values of  $\sigma_0$  have been corrected to a common aperture of 1.53 kpc. The average radii of the extracted apertures are listed in Table 3 of Wolf & Sheinis (2008). (a) The average radius is used for multiple extracted positions (Wolf & Sheinis 2008).

### C. IMAGES, LIGHT PROFILES, & SPECTRA OF THE ULIRG SAMPLE

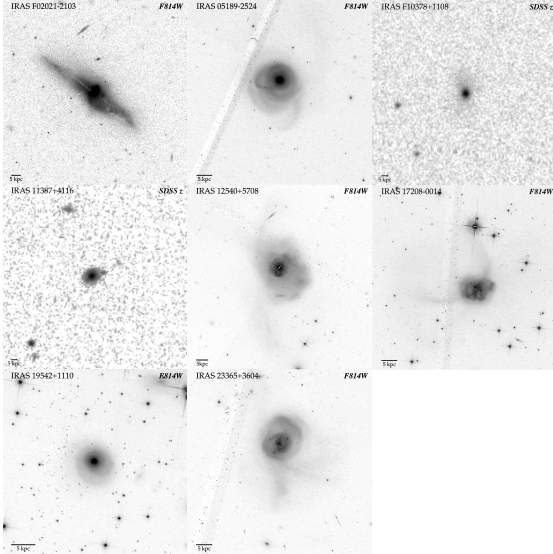


**Figure 1.** HST *F814W* or SDSS *z* images for the 8 advanced ULIRGs. The images are presented in reverse grayscale with a logarithmic stretch. Overplotted on each image is a horizontal solid bar representing 5 kpc. In each image North is up.

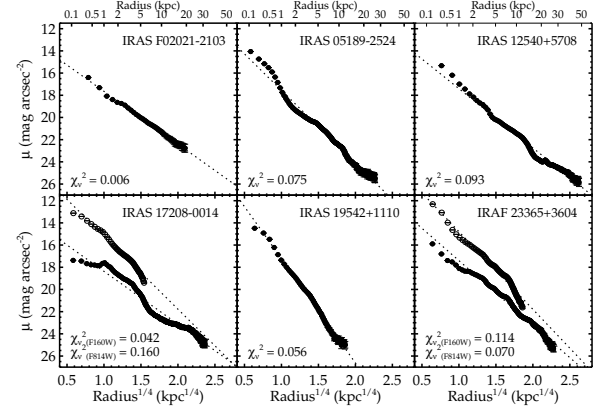


**Figure 2.** Plotted here are the surface brightness profiles in the *F814W*-band (filled circles) for the 6 ULIRGs observed with *HST* using ACS/WFC or WFPC2. Also shown are profiles for two ULIRGs observed with *HST* using the NIC2 camera at *F160W* (open circles).  $1\sigma$  standard errors are over-plotted on each point. The surface brightness profiles are measured out to a S/N=3 over the background. All profiles are measured using circular apertures. The plotted points are equally spaced and linear, corresponding to 3 pixels for ACS, 2 pixels for WFPC2, and 2 pixels for NIC2 (a radius of 9 pixels was used for IRAS 12540+5708 to compensate for the saturated/masked central region). The light dashed line in each plot represents the best-fit de Vaucouleurs  $r^{1/4}$  fit to all of the data. The  $\chi^2_\nu$  of the best fit is shown in each panel. The two profiles plotted in the panels for IRAS 17208-0014 and IRAS 23365+3604 have not been shifted. They represent the actual values. These two ULIRGs also show significantly redder ( $I-H$ ) colors at  $R < 1$  kpc than the value of 1.77-1.79 expected from a typical elliptical galaxy (Frogel et al. 1978; Pahre 1999), consistent with the results from Figure 13 of Paper I.

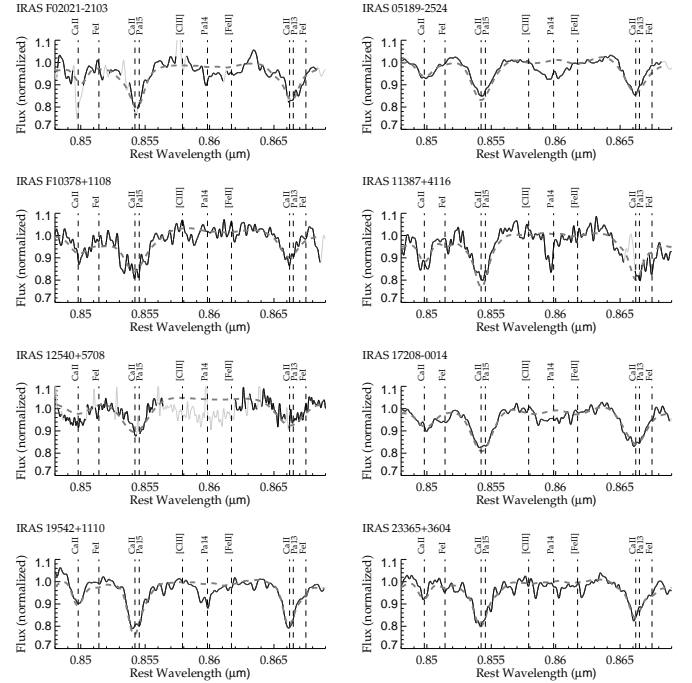


**Figure 3.** Shown here are the CaT spectra of the ULIRGs observed with ESI on Keck-2. The solid black lines show the actual spectrum, the light grey lines show masked bad pixels and/or emission lines. The thick dashed line shows the best-fit convolved template. Also shown are the positions of known emission and absorption lines within the wavelength range (Note: this does not mean that all of these lines are detected.)

**Table 1**  
Summary of KS Tests: Can the Null Hypothesis be Rejected at the 95% level?

Comparison Sample	Fundamental Plane (2D)	$\sigma_o$	$M_{\text{Dyn}}-M/L$ (2D)	$M_{\text{Dyn}}$	Kormendy <sup>a</sup> Relation (2D)	Log $R_{\text{eff}}$ <sup>a</sup>	$\langle\mu_I\rangle_{\text{eff}}$ <sup>a</sup>	Log $L_{\text{IR}}$ ( $L_{\odot}$ )
RLQs	No (89%)	Yes (26%)	Yes <sup>d</sup> (72%)	Yes <sup>e</sup> (87%)	No	No <sup>h</sup>	No	No
RQQs	...	...	...	...	No	No	No	No
All QSOs	No (100%)	No (97%)	Yes (27%)	No (100%)	No	No	No	No
SDSS Ellipticals	Yes <sup>b</sup>	Yes <sup>c</sup>	Yes <sup>b</sup>	Yes <sup>f</sup>	No <sup>g</sup>	No <sup>i</sup>	No	...

**Note.** — This table presents a summary of the 1D and 2D KS tests performed between the distributions of the ULIRGs and the various samples listed in Column 1. The term “2D” refers to the two-dimensional KS test. Otherwise the KS test results presented here are for the standard two-sided KS test which compares the distributions of two empirical samples. Due to the large errors associated with the RLQ  $\sigma_o$  values, the KS tests also have been run using Monte Carlo simulations in which each RLQ  $\sigma_o$  is randomly assigned a value of  $\sigma_o \pm \Delta\sigma_o$ . Test results above which include the RLQ  $\sigma_o$  parameter show a parentheses indicating what percent of 10,000 Monte Carlo simulations the result occurs. Although IRAS 19542+1110 is  $3.9\sigma$  outlier from the FP, excluding it from the KS tests in columns 2-5 does not change the results presented above. (a) Comparison with larger photometric sample of QSOs (28 RLQs and 25 RQQs); (b) No for 165-225 km s<sup>-1</sup> and 225-420 km s<sup>-1</sup> bins; (c) The Null Hypothesis can also be rejected at the 99% level; (d) The Null Hypothesis can also be rejected at the 99% level but only 13% of the time; (e) The Null Hypothesis can also be rejected at the 99% level but only 12% of the time; (f) No for the 225-420 km s<sup>-1</sup> bins; (g) The Null Hypothesis can be rejected when IRAS 19542+1110 is excluded. The Null Hypothesis cannot be rejected for the 165-225 km s<sup>-1</sup> and 225-420 km s<sup>-1</sup> bins whether or not IRAS 19542+1110 is excluded; (h) If only the 6 RLQs in the kinematic sub-sample are compared with the ULIRGs, then the Null Hypothesis can be rejected; (i) When IRAS 19542+1110 is excluded the Null Hypothesis can be rejected.

# D. COSMIC RAY REJECTION ALGORITHM AND BAD PIXEL MASK

Most *HST*/ACS programs employ either CR-SPLIT, (two separate exposures at the same pointing), or multiple (e.g.  $> 2$ ) dithered positions to remove cosmic rays (CRs) and artifacts. The CR-SPLIT mode is most appropriate for programs where the absence of data in the gap will not impact the science (small targets or point sources). MULTIDRIZZLE compares the two images and flags pixels that have changed significantly between the two exposures. Dithering will “fill in” the chip gap and allow for the recovery of information in the chip gap. With at least 3 dither positions the same technique for removing CRs in the chip gap can be used. Program 10592 used a two position dithering scheme (ACS-WFC-DITHER-LINE) that shifts the image 5 pixels in X and 60 pixels in Y. This fills the chip gap but with data from one exposure only (each gap is filled by information from the other exposure). Thus, the final images contained significant CR hits and hot pixels in the chip gap. Because the ULIRGs were not centered on either chip, but centered in the ACS/WFC FOV (aperture WFC) the chip gap runs through the outer regions of the galaxy, impacting the science data. Because more objects were affected by this than in Paper I, an improved and more automated algorithm was developed to create a bad pixel mask. First, a zero level background image was created by identifying the median background flux levels of the multidrizzled final image and replacing pixels at or below these values with a value of zero (using IMREPLACE). Second, the zero-level background image was passed through a median filter using a  $15 \times 15$  pixel filter box, creating a new filtered image. Third, the zero-level background image was divided by the median filtered image. In this divided image, all pixels with flux values above the maximum pixel value in the nucleus were set to a value of 1 (bad), the remaining pixels were set to a value of 0 (good). This pixel mask proved successful for identifying saturated stars, diffraction spikes, and elongated CRs in the gap and areas covered by only one pointing. This pixel mask was then combined with one created from pixels flagged bad by MULTIDRIZZLE, and a pixel mask created from the positions of foreground stars and background galaxies.

## REFERENCES

- Abazajian, K. N. e. a. 2009, ApJS, 182, 543  
 Alladin, S. M. 1965, ApJ, 141, 768  
 Anantharamaiah, K. R., Viallefond, F., Mohan, N. R., Goss, W. M., & Zhao, J. H. 2000, ApJ, 537, 613  
 Armus, L., Mazzarella, J. M., Evans, A. S., Surace, J. A., Sanders, D. B., Iwasawa, K., Frayer, D. T., Howell, J. H., Chan, B., Petric, A., Vavilkin, T., Kim, D. C., Haan, S., Inami, H., Murphy, E. J., Appleton, P. N., Barnes, J. E., Bothun, G., Bridge, C. R., Charmandaris, V., Jensen, J. B., Kewley, L. J., Lord, S., Madore, B. F., Marshall, J. A., Melbourne, J. E., Rich, J., Satyapal, S., Schulz, B., Spoon, H. W. W., Sturm, E., U, V., Veilleux, S., & Xu, K. 2009, PASP, 121, 559  
 Bacon, R., Monnet, G., & Simien, F. 1985, A&A, 152, 315  
 Bahcall, J. N., Kirhakos, S., Saxe, D. H., & Schneider, D. P. 1997, ApJ, 479, 642  
 Baldry, I. K., Glazebrook, K., Brinkmann, J., Ivezić, Ž., Lupton, R. H., Nichol, R. C., & Szalay, A. S. 2004, ApJ, 600, 681  
 Baldry, I. K., Glazebrook, K., & Driver, S. P. 2008, MNRAS, 388, 945  
 Barnes, J. E. 1988, ApJ, 331, 699  
 —. 1992, ApJ, 393, 484  
 —. 2002, MNRAS, 333, 481  
 Barnes, J. E. & Hernquist, L. 1996, ApJ, 471, 115  
 Barnes, J. E. & Hernquist, L. E. 1991, ApJ, 370, L65  
 Barth, A. J., Ho, L. C., & Sargent, W. L. W. 2002, AJ, 124, 2607  
 Bell, E. F. & de Jong, R. S. 2001, ApJ, 550, 212  
 Bell, E. F., McIntosh, D. H., Katz, N., & Weinberg, M. D. 2003, ApJS, 149, 289  
 Bell, E. F., Zheng, X. Z., Papovich, C., Borch, A., Wolf, C., & Meisenheimer, K. 2007, ApJ, 663, 834  
 Bender, R., Burstein, D., & Faber, S. M. 1992, ApJ, 399, 462  
 Bender, R., Surma, P., Doebereiner, S., Moellenhoff, C., & Madejsky, R. 1989, A&A, 217, 35, (B89)  
 Bennert, N., Canalizo, G., Jungwiert, B., Stockton, A., Schweizer, F., Peng, C. Y., & Lacy, M. 2008, ApJ, 677, 846  
 Bernardi, M. 2007, AJ, 133, 1954  
 Bernardi, M., Sheth, R. K., Annis, J., Burles, S., Eisenstein, D. J., Finkbeiner, D. P., Hogg, D. W., Lupton, R. H., Schlegel, D. J., SubbaRao, M., Bahcall, N. A., Blakeslee, J. P., Brinkmann, J., Castander, F. J., Connolly, A. J., Csabai, I., Doi, M., Fukugita, M., Frieman, J., Heckman, T., Hennessy, G. S., Ivezić, Z., Knapp, G. R., Lamb, D. Q., McKay, T., Munn, J. A., Nichol, R., Okamura, S., Schneider, D. P., Thakur, A. R., & York, D. G. 2003a, AJ, 125, 1866  
 —. 2003b, AJ, 125, 1817  
 Bertram, T., Eckart, A., Fischer, S., Zuther, J., Straubmeier, C., Wisotzki, L., & Krips, M. 2007, A&A, 470, 571  
 Binney, J. 1982, ARA&A, 20, 399  
 Blanton, M. R., Hogg, D. W., Bahcall, N. A., Brinkmann, J., Britton, M., Connolly, A. J., Csabai, I., Fukugita, M., Loveday, J., Meiksin, A., Munn, J. A., Nichol, R. C., Okamura, S., Quinn, T., Schneider, D. P., Shimasaku, K., Strauss, M. A., Tegmark, M., Vogeley, M. S., & Weinberg, D. H. 2003, ApJ, 592, 819  
 Bruzual, G. From Stars to Galaxies: Building the Pieces to Build Up the Universe, ed. , A. VallenariR. Tantalol. Portinari & A. Moretti, 303  
 Bruzual, G. 2010, Royal Society of London Philosophical Transactions Series A, 368, 783  
 Bruzual, G. & Charlot, S. 2003, MNRAS, 344, 1000  
 Bryant, P. M. & Scoville, N. Z. 1996, ApJ, 457, 678  
 Calzetti, D., Kinney, A. L., & Storchi-Bergmann, T. 1994, ApJ, 429, 582  
 Canalizo, G., Bennert, N., Jungwiert, B., Stockton, A., Schweizer, F., Lacy, M., & Peng, C. 2007, ApJ, 669, 801  
 Canalizo, G. & Stockton, A. 2000, ApJ, 528, 201  
 —. 2001, ApJ, 555, 719  
 Cappellari, M., Bacon, R., Bureau, M., Damen, M. C., Davies, R. L., de Zeeuw, P. T., Emsellem, E., Falcón-Barroso, J., Krajnović, D., Kuntschner, H., McDermid, R. M., Peletier, R. F., Sarzi, M., van den Bosch, R. C. E., & van de Ven, G. 2006, MNRAS, 366, 1126  
 Chini, R., Kreysa, E., & Wargau, W. F. 1997, A&A, 318, 15  
 Cole, S., Norberg, P., Baugh, C. M., Frenk, C. S., Bland-Hawthorn, J., Bridges, T., Cannon, R., Colless, M., Collins, C., Couch, W., Cross, N., Dalton, G., De Propris, R., Driver, S. P., Efstathiou, G., Ellis, R. S., Glazebrook, K., Jackson, C., Lahav, O., Lewis, I., Lumsden, S., Maddox, S., Madgwick, D., Peacock, J. A., Peterson, B. A., Sutherland, W., & Taylor, K. 2001, MNRAS, 326, 255  
 Colina, L., Arribas, S., & Monreal-Ibero, A. 2005, ApJ, 621, 725  
 Dasyra, K. M., Tacconi, L. J., Davies, R. I., Naab, T., Genzel, R., Lutz, D., Sturm, E., Baker, A. J., Veilleux, S., Sanders, D. B., & Burkert, A. 2006, ApJ, 651, 835  
 Davies, R. I., Tacconi, L. J., & Genzel, R. 2004, ApJ, 613, 781  
 de Jong, R. S. & Bell, E. F. 2007, Comparing Dynamical and Stellar Population Mass-To-Light Ratio Estimates, ed. R. S. de Jong, 107  
 de Vaucouleurs, G. 1953, MNRAS, 113, 134  
 Djorgovski, S. & Davis, M. 1987, ApJ, 313, 59  
 Djorgovski, S., de Carvalho, R., & Han, M.-S. in , Astronomical Society of the Pacific Conference Series, Vol. 4, The Extragalactic Distance Scale, ed. S. van den BerghC. J. Pritchet, 329–341  
 Downes, D. & Solomon, P. M. 1998, ApJ, 507, 615  
 Dunlop, J. S., McLure, R. J., Kukula, M. J., Baum, S. A., O’Dea, C. P., & Hughes, D. H. 2003, MNRAS, 340, 1095  
 Dupraz, C., Casoli, F., Combes, F., & Kazes, I. 1990, A&A, 228, L5  
 Evans, A. S. The Starburst-AGN Connection, ed. , W. WangZ. YangZ. Luo & Z. Chen, 35  
 Evans, A. S., Frayer, D. T., Surace, J. A., & Sanders, D. B. 2001, AJ, 121, 1893  
 Evans, A. S., Hines, D. C., Barthel, P., Schneider, G., Surace, J. A., Sanders, D. B., Vavilkin, T., Frayer, D. T., Tacconi, L. J., & Storrie-Lombardi, L. J. 2009, AJ, 138, 262

- Faber, S. M., Dressler, A., Davies, R. L., Burstein, D., & Lynden-Bell, D. 1987, in *Nearly Normal Galaxies. From the Planck Time to the Present*, ed. S. M. Faber, 175–183
- Fasano, G. & Franceschini, A. 1987, *MNRAS*, 225, 155
- Feigelson, E. D. & Babu, G. J. 1992, *ApJ*, 397, 55
- Feruglio, C., Maiolino, R., Piconcelli, E., Menci, N., Aussel, H., Lamastra, A., & Fiore, F. 2010, *A&A*, 518, L155+
- Fischer, J., Sturm, E., González-Alfonso, E., Graciá-Carpio, J., Hailey-Dunsheath, S., Poglitsch, A., Contursi, A., Lutz, D., Genzel, R., Sternberg, A., Verma, A., & Tacconi, L. 2010, *A&A*, 518, L41
- Fish, R. A. 1964, *ApJ*, 139, 284
- Fisher, R. 1925, *Statistical Methods for Research Workers* (Edinburgh : Oliver & Boyd, 1925)
- , 1990, *Statistical Methods, Experimental Design, and Scientific Inference*. (University Press, 1990)
- Fitzpatrick, E. L. 1999, *PASP*, 111, 63
- Floyd, D. J. E., Kukula, M. J., Dunlop, J. S., McLure, R. J., Miller, L., Percival, W. J., Baum, S. A., & O’Dea, C. P. 2004, *MNRAS*, 355, 196
- Frogl, J. A., Persson, S. E., Matthews, K., & Aaronson, M. 1978, *ApJ*, 220, 75
- Genzel, R., Tacconi, L. J., Rigopoulou, D., Lutz, D., & Tecza, M. 2001, *ApJ*, 563, 527
- Gerhard, O., Kronawitter, A., Saglia, R. P., & Bender, R. 2001, *AJ*, 121, 1936
- Greve, T. R., Papadopoulos, P. P., Gao, Y., & Radford, S. J. E. 2009, *ApJ*, 692, 1432
- Guyon, O., Sanders, D. B., & Stockton, A. 2006, *ApJS*, 166, 89
- Haan, S., Surace, J. A., Armus, L., Evans, A. S., Howell, J. H., Mazzarella, J. M., Kim, D. C., Vavilkin, T., Inami, H., Sanders, D. B., Petric, A., Bridge, C. R., Melbourne, J. L., Charmandaris, V., Diaz-Santos, T., Murphy, E. J., U, V., Stierwalt, S., & Marshall, J. A. 2011, *AJ*, 141, 100
- Haas, M., Klaas, U., Müller, S. A. H., Bertoldi, F., Camenzind, M., Chini, R., Krause, O., Lemke, D., Meisenheimer, K., Richards, P. J., & Wilkes, B. J. 2003, *A&A*, 402, 87
- Haas, M., Müller, S. A. H., Chini, R., Meisenheimer, K., Klaas, U., Lemke, D., Kreysa, E., & Camenzind, M. 2000, *A&A*, 354, 453
- Hamabe, M. & Kormendy, J. in , *IAU Symposium, Vol. 127. Structure and Dynamics of Elliptical Galaxies*, ed. P. T. de Zeeuw, S. D. Tremaine, 379
- Hamilton, T. S., Casertano, S., & Turnshek, D. A. 2002, *ApJ*, 576, 61
- , 2008, *ApJ*, 678, 22
- Heckman, T. M., Smith, E. P., Baum, S. A., van Breugel, W. J. M., Miley, G. K., Illingworth, G. D., Bothun, G. D., & Balick, B. 1986, *ApJ*, 311, 526
- Herschel, W. 1786, *Royal Society of London Philosophical Transactions Series I*, 76, 457
- Hibbard, J. E. & van Gorkom, J. H. 1996, *AJ*, 111, 655
- Hill, D. T., Driver, S. P., Cameron, E., Cross, N., Liske, J., & Robotham, A. 2010, *MNRAS*, 404, 1215
- Hjorth, J. & Madsen, J. 1991, *MNRAS*, 253, 703
- Holmberg, E. 1941, *ApJ*, 94, 385
- Holtzman, J. A., Hester, J. J., Casertano, S., Trauger, J. T., Watson, A. M., Ballester, G. E., Burrows, C. J., Clarke, J. T., Crisp, D., Evans, R. W., Gallagher, III, J. S., Griffiths, R. E., Hoessel, J. G., Matthews, L. D., Mould, J. R., Scowen, P. A., Stapelfeldt, K. R., & Westphal, J. A. 1995, *PASP*, 107, 156
- Hooper, E. J., Impey, C. D., Foltz, C. B., & Hewett, P. C. 1995, *ApJ*, 445, 62
- Hopkins, P. F., Hernquist, L., Cox, T. J., Di Matteo, T., Robertson, B., & Springel, V. 2006, *ApJS*, 163, 1
- Hopkins, P. F., Hernquist, L., Cox, T. J., Dutta, S. N., & Rothberg, B. 2008, *ApJ*, 679, 156
- Horne, K. *New Directions in Spectrophotometry*, ed. , A. G. D. Philip, D. S. Hayes & S. J. Adelman, 145
- Hubble, E. P. 1930, *ApJ*, 71, 231
- Hughes, D. H., Kukula, M. J., Dunlop, J. S., & Boroson, T. 2000, *MNRAS*, 316, 204
- Hutchings, J. B. & Neff, S. G. 1988, *AJ*, 96, 1575
- , 1992, *AJ*, 104, 1
- Hyde, J. B. & Bernardi, M. 2009a, *MNRAS*, 394, 1978
- , 2009b, *MNRAS*, 396, 1171
- Impey, C. D. & Neugebauer, G. 1988, *AJ*, 95, 307
- Iono, D., Yun, M. S., & Ho, P. T. P. 2005, *ApJS*, 158, 1
- James, P., Bate, C., Wells, M., Wright, G., & Doyon, R. 1999, *MNRAS*, 309, 585
- Jorgensen, I., Franx, M., & Kjaergaard, P. 1995, *MNRAS*, 276, 1341
- , 1996, *MNRAS*, 280, 167
- Joseph, R. D. 1999, *Ap&SS*, 266, 321
- Kauffmann, G., Heckman, T. M., White, S. D. M., Charlot, S., Tremonti, C., Peng, E. W., Seibert, M., Brinkmann, J., Nichol, R. C., SubbaRao, M., & York, D. 2003, *MNRAS*, 341, 54
- Kennicutt, Jr., R. C. 1998, *ARA&A*, 36, 189
- Kim, D. & Sanders, D. B. 1998, *ApJS*, 119, 41
- Kinney, A. L., Calzetti, D., Bohlin, R. C., McQuade, K., Storchi-Bergmann, T., & Schmitt, H. R. 1996, *ApJ*, 467, 38
- Koornneef, J., Bohlin, R., Buser, R., Horne, K., & Turnshek, D. 1986, *Highlights of Astronomy*, 7, 833
- Kormendy, J. 1977, *ApJ*, 218, 333
- Kormendy, J. in , *Saas-Fee Advanced Course 12: Morphology and Dynamics of Galaxies*, ed. L. Martinet, M. Mayor, 113–288
- Laidler, V., Bushouse, H., Simon, B., & Bazell, D. 2005
- Letawe, G., Magain, P., Courbin, F., Jablonka, P., Jahnke, K., Meylan, G., & Wisotzki, L. 2007, *MNRAS*, 378, 83
- Lutz, D. 1991, *A&A*, 245, 31
- Lynden-Bell, D. 1967, *MNRAS*, 136, 101
- MacKenty, J. W. & Stockton, A. 1984, *ApJ*, 283, 64
- Maraston, C. 2005, *MNRAS*, 362, 799
- Maraston, C., Daddi, E., Renzini, A., Cimatti, A., Dickinson, M., Papovich, C., Pasquali, A., & Pirzkal, N. 2006, *ApJ*, 652, 85
- Massey, F. J. 1951, *Journal of the American Statistical Association*
- Mathews, W. G. 1988, *AJ*, 95, 1047
- McCall, M. L. 2004, *AJ*, 128, 2144
- McLure, R. J., Kukula, M. J., Dunlop, J. S., Baum, S. A., O’Dea, C. P., & Hughes, D. H. 1999, *MNRAS*, 308, 377
- Mihos, C. 1999, *Ap&SS*, 266, 195
- Mihos, J. C. & Hernquist, L. 1994a, *ApJ*, 437, L47
- , 1994b, *ApJ*, 431, L9
- , 1996, *ApJ*, 464, 641
- Miller, L., Peacock, J. A., & Mead, A. R. G. 1990, *MNRAS*, 244, 207
- Milvang-Jensen, B. & Jørgensen, I. 1999, *Baltic Astronomy*, 8, 535
- Moshir, M. & et al. 1990, in *IRAS Faint Source Catalogue, version 2.0 (1990)*, 0–+
- Nigoche-Netro, A., Moles, M., Ruelas-Mayorga, A., Franco-Balderas, A., & Kjergaard, P. 2007, *A&A*, 472, 773
- Nigoche-Netro, A., Ruelas-Mayorga, A., & Franco-Balderas, A. 2008, *A&A*, 491, 731
- , 2009, *MNRAS*, 392, 1060
- Nolan, L. A., Dunlop, J. S., Kukula, M. J., Hughes, D. H., Boroson, T., & Jimenez, R. 2001, *MNRAS*, 323, 308
- O’Dowd, M., Urry, C. M., & Scarpa, R. 2002, *ApJ*, 580, 96
- Pahre, M. A. 1999, *ApJS*, 124, 127
- Pahre, M. A., de Carvalho, R. R., & Djorgovski, S. G. 1998a, *AJ*, 116, 1606
- Pahre, M. A., Djorgovski, S. G., & de Carvalho, R. R. 1998b, *AJ*, 116, 1591
- Peacock, J. A. 1983, *MNRAS*, 202, 615
- Pearson, E. S. & Hartley, H. O. 1972, *Biometrika Tables for Statisticians, Vol. 2, 2nd ed.*, ed. , Vol. 2
- Pease, F. G. 1917, *ApJ*, 46, 24
- , 1920, *ApJ*, 51, 276
- Perrine, C. D. 1922, *MNRAS*, 82, 486
- Press, W. H., Teukolsky, S. A., Vetterling, W. T., & Flannery, B. P. 1992, *Numerical recipes in FORTRAN. The art of scientific computing* (Cambridge: University Press, 1992, 2nd ed.)
- Prestwich, A. H., Joseph, R. D., & Wright, G. S. 1994, *ApJ*, 422, 73
- Proveda, A. 1958, *Bal. Obs. Tonantzintla y Tacubaya*, 17, 3
- Ramos Almeida, C., Tadhunter, C. N., Inskip, K. J., Morganti, R., Holt, J., & Dicken, D. 2011, *MNRAS*, 410, 1550
- Reda, F. M., Forbes, D. A., Beasley, M. A., O’Sullivan, E. J., & Goudfroij, P. 2004, *MNRAS*, 354, 851
- Redman, R. O. & Shirley, E. G. 1938, *MNRAS*, 98, 613
- Richstone, D. O. & Tremaine, S. 1986, *AJ*, 92, 72
- Rix, H. & White, S. D. M. 1992, *MNRAS*, 254, 389
- Rood, H. J., Page, T. L., Kintner, E. C., & King, I. R. 1972, *ApJ*, 175, 627
- Rosse, L. 1850, *Philosophical Transactions of the Royal Society*, 140, 499
- Rothberg, B. 2009, in *Astronomical Society of the Pacific Conference Series, Vol. 419, Astronomical Society of the Pacific Conference Series*, ed. S. Jogee, I. Marinova, L. Hao, & G. A. Blanc, 273–+
- Rothberg, B. & Fischer, J. *Galaxy Wars: Stellar Populations and Star Formation in Interacting Galaxies*, ed. , B. Smith, J. Higdon, S. Higdon & N. Bastian, 351
- Rothberg, B. & Fischer, J. 2010b, *ApJ*, 712, 318
- Rothberg, B. & Joseph, R. D. 2004, *AJ*, 128, 2098
- , 2006a, *AJ*, 131, 185
- , 2006b, *AJ*, 132, 976
- Rupke, D. S., Veilleux, S., & Sanders, D. B. 2002, *ApJ*, 570, 588
- Sanders, D. B. 1999, *Ap&SS*, 266, 331
- Sanders, D. B., Mazzarella, J. M., Kim, D.-C., Surace, J. A., & Soifer, B. T. 2003, *AJ*, 126, 1607
- Sanders, D. B. & Mirabel, I. F. 1996, *ARA&A*, 34, 749

- Sanders, D. B., Phinney, E. S., Neugebauer, G., Soifer, B. T., & Matthews, K. 1989a, *ApJ*, 347, 29
- Sanders, D. B., Scoville, N. Z., Zensus, A., Soifer, B. T., Wilson, T. L., Zylka, R., & Steppe, H. 1989b, *A&A*, 213, L5
- Sanders, D. B., Soifer, B. T., Elias, J. H., Madore, B. F., Matthews, K., Neugebauer, G., & Scoville, N. Z. 1988, *ApJ*, 325, 74
- Schlafly, E. F. & Finkbeiner, D. P. 2011, *ApJ*, 737, 103
- Schlegel, D. J., Finkbeiner, D. P., & Davis, M. 1998, *ApJ*, 500, 525
- Schweizer, F. 1982, *ApJ*, 252, 455
- , 1996, *AJ*, 111, 109
- Schweizer, F. & Seitzer, P. 2007, *AJ*, 133, 2132
- Scoville, N. Z., Frayer, D. T., Schinnerer, E., & Christopher, M. 2003, *ApJ*, 585, L105
- Scoville, N. Z., Yun, M. S., & Bryant, P. M. 1997, *ApJ*, 484, 702
- Sheinis, A. I., Bolte, M., Epps, H. W., Kibrick, R. I., Miller, J. S., Radovan, M. V., Bigelow, B. C., & Sutlin, B. M. 2002, *PASP*, 114, 851
- Shier, L. M. & Fischer, J. 1998, *ApJ*, 497, 163
- Shier, L. M., Rieke, M. J., & Rieke, G. H. 1996, *ApJ*, 470, 222
- Smith, D. A., Herter, T., Haynes, M. P., Beichman, C. A., & Gautier, III, T. N. 1995, *ApJ*, 439, 623
- Soifer, B. T., Sanders, D. B., Neugebauer, G., Danielson, G. E., Lonsdale, C. J., Madore, B. F., & Persson, S. E. 1986, *ApJ*, 303, L41
- Solomon, P. M., Downes, D., & Radford, S. J. E. 1992, *ApJ*, 387, L55
- Solomon, P. M., Downes, D., Radford, S. J. E., & Barrett, J. W. 1997, *ApJ*, 478, 144
- Springel, V. 2000, *MNRAS*, 312, 859
- Stephens, M. A. 1970, *Journal of the Royal Statistical Society. Series B (Methodological)*, 32, 115 [LINK]
- Stoeke, J. T., Morris, S. L., Weymann, R. J., & Foltz, C. B. 1992, *ApJ*, 396, 487
- Sturm, E., González-Alfonso, E., Veilleux, S., Fischer, J., Graciá-Carpio, J., Hailey-Dunsheath, S., Contursi, A., Poglitsch, A., Sternberg, A., Davies, R., Genzel, R., Lutz, D., Tacconi, L., Verma, A., Maiolino, R., & de Jong, J. A. 2011, *ApJ*, 733, L16
- Surace, J. A., Sanders, D. B., Vacca, W. D., Veilleux, S., & Mazzarella, J. M. 1998, *ApJ*, 492, 116
- Tacconi, L. J., Genzel, R., Lutz, D., Rigopoulou, D., Baker, A. J., Iserlohe, C., & Tecza, M. 2002, *ApJ*, 580, 73
- Tadhunter, C., Holt, J., González Delgado, R., Rodríguez Zaurín, J., Villar-Martín, M., Morganti, R., Emonts, B., Ramos Almeida, C., & Inskip, K. 2011, *MNRAS*, 412, 960
- Tolman, R. C. 1930, *Proceedings of the National Academy of Science*, 16, 511
- Tonry, J. L. & Davis, M. 1981, *ApJ*, 246, 680
- Toomre, A. 1977, in *Evolution of Galaxies and Stellar Populations*, p. 401
- Toomre, A. & Toomre, J. 1972, *ApJ*, 178, 623
- Trentham, N., Kormendy, J., & Sanders, D. B. 1999, *AJ*, 117, 2152
- Tukey, J. W. 1958, *The Annals of Mathematical Statistics*
- van der Marel, R. P. & Franx, M. 1993, *ApJ*, 407, 525
- Vanderbeke, J., Baes, M., Romanowsky, A. J., & Schmidtobreick, L. 2011, *MNRAS*, 412, 2017
- Veilleux, S., Kim, D., Rupke, D. S. N., Peng, C. Y., Tacconi, L. J., Genzel, R., Lutz, D., Sturm, E., Contursi, A., Schweitzer, M., Dasyra, K. M., Ho, L. C., Sanders, D. B., & Burkert, A. 2009, *ApJ*, 701, 587
- Veilleux, S., Kim, D., & Sanders, D. B. 2002, *ApJS*, 143, 315
- Veilleux, S., Kim, D.-C., Peng, C. Y., Ho, L. C., Tacconi, L. J., Dasyra, K. M., Genzel, R., Lutz, D., & Sanders, D. B. 2006, *ApJ*, 643, 707
- Wang, Z., Scoville, N. Z., & Sanders, D. B. 1991, *ApJ*, 368, 112
- Whitmore, B. C., Schweizer, F., Leitherer, C., Borne, K., & Robert, C. 1993, *AJ*, 106, 1354
- Wold, I., Sheinis, A. I., Wolf, M. J., & Hooper, E. J. 2010, *MNRAS*, 408, 713
- Wolf, M. J. & Sheinis, A. I. 2008, *AJ*, 136, 1587
- Wright, A. E. 1972, *MNRAS*, 157, 309
- Wright, G. S., James, P. A., Joseph, R. D., & McLean, I. S. 1990, *Nature*, 344, 417
- Xia, X. Y., Gao, Y., Hao, C.-N., Tan, Q. H., Mao, S., Omont, A., Flaquer, B. O., Leon, S., & Cox, P. 2012, *ApJ*, 750, 92
- Yip, C. W., Connolly, A. J., Szalay, A. S., Budavári, T., SubbaRao, M., Frieman, J. A., Nichol, R. C., Hopkins, A. M., York, D. G., Okamura, S., Brinkmann, J., Csabai, I., Thakar, A. R., Fukugita, M., & Ivezić, Ž. 2004, *AJ*, 128, 585
- York, D. G. et al. 2000, *AJ*, 120, 1579
- Yun, M. S., Reddy, N. A., & Condon, J. J. 2001, *ApJ*, 554, 803
- Zwicky, F. 1956, *Ergebnisse der exakten Naturwissenschaften*, 29, 344